九州大学学術情報リポジトリ
Kyushu University Institutional Repository

Stratigraphy, petrology, and geochemistry of a Neoproterozoic banded iron sequence in the El-Dabbah Group, Central Eastern Desert, Egypt

Kiyokawa, Shoichi
Department of Earth and Planetary Science, Kyushu University

Suzuki, Taishi
Department of Earth and Planetary Science, Kyushu University

Hanaa Abdenaby El-Dokouny
Department of Geology, Faculty of Science, Menoufiya University

Al-Dekouny Maher Dawoud
Department of Geology, Faculty of Science, Menoufiya University

他

https://hdl.handle.net/2324/4061288

出版情報：Journal of African Earth Sciences. 168, pp.103805-, 2020-08. Elsevier
バージョン：
権利関係：

KYUSHU UNIVERSITY

Stratigraphy, petrology, and geochemistry of a Neoproterozoic banded iron sequence in the El-Dabbah Group, Central Eastern Desert, Egypt

Shoichi Kiyokawa[a,b,c], Taishi Suzuki[a], Hanna El-Dokounyd[d], Al-Dekouny Maher Dawoud[d], Mohamed Mahmoud El-Hasan[d]

[a] Department of Earth and Planetary Science, Kyushu University, 744 Motooka Nishiku, Fukuoka 819-0395, Japan

[b] Department of Geology, University of Johannesburg, PO Box 524, Auckland Park, Johannesburg 2006, South Africa

[c] Center for advanced Marine core research, Kochi University, B200 Monobe, Nankoku, Kochi, 783-8502, Japan

[d] Department of Geology, Faculty of Science, Menoufiya University, Gamal Abd El Nasr st. Shebin El-Kom, Menoufiya, Egypt

Corresponding author

Shoichi Kiyokawa: kiyokawa@geo.kyushu-u.ac.jp

Tel.: 092-802-4254

Email addresses

Taishi Suzuki: t14851295@gmail.com

Kenji Horie: horie.kenji@nipr.ac.jp

Mami Takehara: takehara.mami@nipr.ac.jp

Al-Dekouny Maher Dawoud: dawoud_99@yahoo.com

Mohamed Mahmoud El-Hasan: abouelhassanmohamed@gmail.com

Hanna El-Dokouny: hanaaabdelnaby4@gmail.com

Abstract

The El-Dabbah Group of the Nubian Shield, Central Eastern Desert, Egypt, contains a Neoproterozoic banded iron sequence within volcaniclastic rocks deposited in an island arc setting. The group contains a volcaniclastic sequence of relatively undeformed lower-greenschist-facies rocks that are unconformably overlain by terrestrial sedimentary strata of the Hamamat Group. The group is >7000 m thick and contains three formations (the Lower, Middle, and Upper El-Dabbah formations), which include massive metavolcanic rocks, pillow lavas, well-bedded volcaniclastic rocks, black and greenish shale and banded iron sequences. There is no evidence of glaciation, such as diamictites or cap-carbonate beds, in the three formations. The Middle El-Dabbah Formation (2000 m thick) contains well-preserved iron sequences within the volcaniclastic rocks. Most of the iron sequences comprise beds that are a few meters thick. The iron sequence rocks have low contents of Al, Ti, K, and Na, and low Al/(Al+Fe+Mn+Na+K+Ca) ratios, which suggest there was no continental input. Heavy rare earth element enrichment and the absence of Eu anomalies indicate these rocks formed from low-temperature hydrothermal fluids or in a distal setting from a hydrothermal vent system. $\delta^{13}C$ values of the black shales are ca. −22‰, suggesting the organic matter was derived from cyanobacterial activity. Given that several black shale units were precipitated below the iron sequences, the cyanobacterial activity might have produced the oxygen at the ocean surface that led to iron oxidation and deposition. Based on the stratigraphic and geochemical characteristics of the El-Dabbah Group, we propose the iron sequences were deposited in a small isolated basin within the central rift zone of an oceanic island arc. The relationship between the El-Dabbah Group and Sturtian glaciation remains unclear.

Keywords: Central Eastern Desert of Egypt, El-Dabbah Group, Neoproterozoic iron formation, oceanic island arc, black shale, Sturtian glaciation

Highlights:

- Nine banded iron sequences occur in a volcaniclastic sequence of oceanic island arc.
- The iron sequences comprise fine-grained iron oxide and greenish to black shales
- The LREE pattern and no Eu anomaly shows low temperature origin iron sequences.

1. Introduction

Banded iron formations (BIFs) are widely considered to have been produced by the decreasing solubility of iron associated with seawater oxygenation during the ca. 2.45 and 2.20 Ga Great Oxidation Events (GOEs; Holland, 1983; Bekker et al., 2004; Bekker and Kaufman, 2007). BIFs are classified as

Algoma-, Superior-, and Rapitan-types (Gross, 1980). The Algoma-type BIF is hosted within volcanogenic rocks and the Superior-type BIF is hosted within continental shelf sedimentary rocks. During the Neoproterozoic, iron formations re-appeared in the sedimentary record in several places (Lsley and Abbott, 1999; Klein, 2005). The Rapitan-type BIFs are associated with Neoproterozoic glacial deposits at several localities (e.g., Young, 1976; James, 1983; Klein and Beukes, 1993; Klein and Ladeira, 2004; Cox et al., 2013) and may have been related to Snowball Earth events (e.g., Kirschivink, 1992; Klein and Beukes, 1993; Hoffman et al., 1998). However, at several localities, are is no geological evidence for glaciation at this time (Cox et al., 2013; Abd El-Rahman et al., 2019). Continental reconstructions have suggested that Neoproterozoic iron formations (NIFs) were deposited in rift basins associated with the break-up of Rodinia (Cox et al., 2013). This continental rift tectonism (i.e., the zipper-rift model) and associated hydrothermal activity may have led to iron sedimentation (e.g., Eyles and Januszczak, 2004; Basta et al., 2011; Cox et al., 2013; Gaucher et al., 2015). The depositional ages of these NIFs vary from Cryogenian to Sturtian (760–630 Ma; e.g., Cox et al., 2013; Gaucher et al., 2015).

In the Central Eastern Desert (CED) of Egypt, there are non-glacial iron sequences that were deposited in a non-rift setting within an island arc volcaniclastic sequence (e.g., Khalil and El-Shazly, 2014; Khalil et al., 2015; Abd El-Rahman et al., 2019). These iron sequences may have formed by three mechanisms: (1) chemical precipitation on a continental shelf with the iron source being continental (e.g., El Aref et al., 1993); (2) precipitation following submarine volcanism and hydrothermal activity in an island arc setting (e.g., El Habaak, 2004; El-Shazly and Khalil, 2014; Abd El-Rahman et al., 2019); or (3) melting of glacial ice during an interglacial period of the Snowball Earth, which is consistent with the presence of some minor diamictite beds within the volcaniclastic sequences (Ali et al., 2010; Stern et al., 2013). Which of these models applies to the iron sequences in the CED of Egypt remains controversial (e.g., Besta et al., 2011; El-Shazly and Khalil, 2016; Abd El-Rahman et al., 2019).

The CED is divided into the North, Central, and South Deserts (NED, CED, and SED, respectively) (e.g., Stern and Hedge, 1985; Fowler and Hamimi, 2019). The NED and CED contain NIFs in island arc volcaniclastic sequences (e.g., Abd El-Rahman et al., 2012; El-Shazly et al., 2019). Depositional ages have been obtained in the Gebel El Hadid area of the southern CED (717 ± 8 Ma basaltic lapilli tuff; Khalil et al., 2015) in the Wadi Hamama area of the western CED (693.0 ± 4.1 Ma dacite tuff; 696.0 ± 2.9 Ma dacite cobble; Abd El-Rahman et al., 2019). These age data indicate the NIFs in the CED were deposited from 720 to 670 Ma, which coincides with the Neoproterozoic Sturtian glaciation (e.g., Stern et al., 2013; Khalil et al., 2015). Only limited evidence of glaciation has been reported in the CED, in the form of small-scale diamictites, including in the Wadi Kareim, Wadi Mobark, and Nuwaybah formations (Ali et al., 2010; Basta et al., 2011; El-Shazly and Khalil, 2014; Khalil et al., 2015; El-Shazly and Khalil, 2016). However, these areas have a complex stratigraphy and the stratigraphic relationships between the diamictites and NIFs are poorly constrained due to a lack of exposure.

El-Shazly et al. (2019) reported geochemical data for 132 samples of NIFs in the CED. Fifty-seven analyses of several NIFs indicated that each NIF formed in a small basin associated with a hydrothermal vent system in an oceanic island arc setting. These areas have not been studied from a geological or stratigraphic perspective (e.g., Abd El-Rahman et al., 2019). As such, the depositional model for the NIFs in the CED is controversial, and their origin may have been related to the Snowball Earth or an Algoma-type setting. It is important to document in detail the stratigraphy of each NIF because of the intense deformation that has occurred in the CED area, including thrust, normal, and strike-slip faulting (e.g., Abd El-Rahman et al., 2019; Mamimi et al., 2019; Kiyokawa et al., in review).

This study was conducted in the El-Dabbah area of the CED, where low-grade metamorphic volcaniclastic rocks are associated with several NIFs (e.g., Ali et al., 2009; El-Shazly and Khalil, 2016). Kiyokawa et al. (in review) undertook detailed geological mapping and stratigraphic reconstructions in this area and identified the El-Dabbah Group (a ~7000-m-thick volcaniclastic sequence). Based on the stratigraphic interpretation, the El-Dabbah Group was proposed to have been deposited in a rift zone within an oceanic island arc (Kiyokawa et al., in review). Here we present detailed stratigraphic, lithological, and petrological observations, and geochemical data for the NIFs and associated rocks, in order to constrain the depositional environment of the El-Dabbah Group.

2. Overview of iron formations in the CED

In the Eastern Desert, 13 occurrences of NIFs have been documented within metavolcanic sequences (Fig. 1; Sims and James, 1984; El Habaak and Soliman, 1999; Basta et al., 2000, 2011; Khalil et al., 2015). In the Eastern Desert, the NIFs are distinct from the extensively documented Archean and Paleoproterozoic BIFs. NIFs only exhibit weak banding and comprise ferruginous laminated siltstone, which does not have clear silica–iron banding. The NIFs contain layers of hematite (Fe_2O_3) and jaspilite (i.e., iron-rich chert) (e.g., Cox et al., 2013). The petrology and geochemistry of the NIFs in the Wadi Kareim and Um Anab areas suggest these are not related to the Snowball Earth, but rather to low temperature hydrothermal activity and volcanism during Rodinia break-up at 800–700 Ma (Basta et al., 2011). These iron formations were likely formed by Algoma-type sedimentation with associated low-temperature hydrothermal activity (Sims and James, 1984). However, there is evidence for glacial activity in the Wadi Kareim, Wadi Mobark, and Nuwaybah formations (Ali et al., 2010; Stern et al., 2013; Khalil et al., 2015).

Metamorphic conditions in the CED ranged from 520 ± 30°C and 5 ± 2 kbar at Um Nar in the south to 400 ± 50°C and 4 ± 2 kbar in the northern areas of Wadi Kareim and Abu Marwat (El-Shazly and Khalil, 2014, 2016). The NIFs and related metavolcanic rocks in Um Nar areas are strongly foliated and metamorphosed, such that the primary bedding, other sedimentary structures, and original stratigraphy are obscured.

3. Geological setting of the El-Dabbah Group

In the Wadi El-Dabbah area, the volcaniclastic rocks and NIFs underwent low-grade metamorphism (lower greenschist facies) and are relatively undeformed (Basta et al., 2011; El-Shazly and Khalil, 2014; Khalil et al., 2015; El-Shazly and Khalil, 2016). Therefore, the strata in this area preserve a coherent stratigraphy and primary sedimentary structures. These strata were identified as the El-Dabbah Group by Kiyokawa et al. (in review), and were considered to represent a Pan-African nappe sequence or accreted island arc sections in previous studies (e.g., Ali et al., 2009; El-Shazly and Khalil, 2016).

The El-Dabbah Group is located between the El-Sibai gneissic complex (i.e., the El-Sibai core complex) and the Kareim Basin. It is unconformably overlain by the Hammamat Group that was deposited in the Kareim Basin (Fritz and Messner, 1999; Ali et al., 2009), and is bounded by a strongly foliated metasedimentary sequence at its eastern and western margins (Atshan Formation; Kiyokawa et al., in review).

The El-Dabbah Group is subdivided into four differently sized domains, which are the northeast (NE), southeast (SE), northwest (NW), and southwest (SW) domains (Fig. 2). Each domain is fault-bounded by the N–S-trending, sinistral El-Dabbah Fault, and E–W-trending and N-dipping normal faults (Kiyokawa et al., in review). The four domains have mostly well-preserved and continuous stratigraphic sequences. Some strata record thrusting sub-parallel to bedding. However, the stratigraphy is relatively undisturbed (Kiyokawa et al., in review). The N-dipping normal fault indicates that the two northern domains contain the upper stratigraphic parts of the El-Dabbah Group. We have reconstructed and correlated the stratigraphy in each domain (Kiyokawa et al., in review). In the present study, we identified and named each iron sequence (NW1 in the NW domain; SE1, 2, and 3 in the SE domain; SW1, 2, 3a, 3b, 4, 5a, 5b, 6, 7, and 8 in the SW domain). At least, nine iron sequences are present throughout the whole stratigraphic sequence. Notably, the Middle El-Dabbah Formation contains seven iron sequences. Three iron sequences (SE1, 2, and 3) in the SE domain can be correlated to iron sequences in the SW domain.

4. Stratigraphy of the El-Dabbah Group

The El-Dabbah Group is divided into the Lower, Middle, and Upper El-Dabbah (ED) formations (Fig. 3). Comparison of the strata in each domain was only conducted for key beds in the banded iron and thick pillow basalt sequences. The thicknesses of each of the three formations are approximate, given the incompletely exposed sections.

The Lower El-Dabbah Formation is distributed in the middle to southern parts of the SE domain and southern part of the SW domain, has a total thickness of ~2000 m, and consists of massive basaltic rocks interlayered with a thin volcaniclastic sequence. The basal contact of this formation is not clear, because the stratigraphically lowest part is an intrusive contact with a hornblende–biotite granite. The thick massive basaltic rocks comprise fine-grained diabase and microgabbro. The upper part of this formation

contains pale greenish shale and thin beds of magnetite-rich iron sequences (location SW1; Fig. 3). Well-preserved massive pillow basalts without vesicles and thin graded greenish shales (i.e., tuffs) suggest the younging direction is to the north.

The Middle El-Dabbah Formation is distributed in the northern SE and SW domains, has a total thickness of ~2500 m, and contains basal massive lava flows and thickly bedded metavolcanic rocks, along with several fine-grained sedimentary sequences. Lava flows and pillow lavas contain small vesicular and amygdaloidal structures in their upper and outer parts, respectively. A thick succession of volcaniclastic rocks and pillow lavas is banded on a scale of 10–40 m. Pillow lava tube morphology and graded bedding of greenish shales (i.e., tuffs) suggest the younging direction is to the north. The sedimentary sequences within these volcaniclastic rocks are also well-preserved, and include finely laminated volcanogenic sediments, black shales, and laterally continuous IFs (Fig. 4A). The iron sequences are interbedded with well-preserved, finely laminated, greenish and black shales (Fig. 4B–C). Each iron sequence is 50 cm–5 m thick.

The Upper El-Dabbah Formation is distributed in the NE and NW domains, has a total thickness of at least 1000 m, and consists of bedded and cross-stratified, fine-grained volcaniclastic rocks and minor pillow lavas that are in conformable contact. Thin iron sequences and black shales are interbedded with greenish volcaniclastic rocks and pillow lavas. The upper part of the Upper El-Dabbah Formation is marked by an unconformity with the overlying Hammamat Group and, in places, an unconformity with the Atshan Formation (Kiyokawa et al., in review).

5. Features of the iron sequences in each domain

The iron sequences are observed in every domain of the El-Dabbah Group. The NE and NW domains contain <5-cm-thick iron sequences within a volcaniclastic sequence. The SE and SW domains contain well-preserved iron sequences within several volcaniclastic sequences. In the SE domain, iron sequences are present within a well-bedded volcaniclastic sequence in the north, and well-preserved iron sequences crop out in a cliff along the eastern side of Wadi El-Dabbah. Several-meter-thick iron sequences in the SE domain are deformed along the El-Dabbah Fault, and these sequences appear to extend into the SW domain.

In the SW domain, well-exposed and laterally continuous iron sequences can be used to reconstruct the stratigraphy (Figs 3 and 5). We constructed five detailed stratigraphic sections, labelled SW1 to SW5a (Figs 3 and 5). These iron sequences are interbedded with greenish and black shales and volcaniclastic rocks, which are exposed along wadi branches of RW12 and RW13, and extend into Wadi El-Dabbah between the RW11 and RW12 areas at old iron mine (Fig. 2). The iron sequences are laminated on a scale of a few centimeters to several meters. The boundaries between the shales and iron sequences are gradational (Fig. 4B) and characterized by increasing amounts of magnetite-rich beds (Fig. 4C).

Section SW1 in the upper part of the Lower El-Dabbah Formation contains the first appearance of iron sequences in the El-Dabbah Group (Fig. 5). The iron sequence is located above a thick massive lava flow and consists of fine-grained magnetite interbedded with greenish siliceous shales. The total thickness of the iron sequence is 4 m. Above this section, thick and fine-grained volcaniclastic rocks are present.

Section SW3a is in the middle part of the Middle El-Dabbah Formation, ~800 m above the SW1 section, and consists of a pale greenish siliceous shale and banded iron bed, which is ~20 m thick and interbedded with volcaniclastic rocks (Figs 4B and 5). Nine thin iron sequences were identified, which are a few centimeters to 2 m thick, and interbedded with laminated, volcaniclastic, silty to sandy, greenish shales. Within each iron bed, the lithology changes gradually from greenish siliceous shale to black iron-rich material (magnetite), indicating that the iron content gradually increases upward through the whole of this formation (Fig. 4B).

Section SW4 is ~15 m thick, located ~100 m above the SW3a section, and comprises lower greenish and black shale and an upper iron sequence (Figs 4C and 5). This section rests on massive basaltic lava flows and is overlain by volcaniclastic rocks. The lower greenish and black shales have load casts and wavy laminations, and are interbedded with a thin graded white tuff (Fig. 4D). The greenish shale consists mainly of silt-sized detrital plagioclase and organic matter (Fig. 4E). The upper iron sequence (ca. 5 m thick) comprises 5–10-cm-thick, well-bedded, magnetite- and hematite-rich layers that are interbedded with thin dark greenish siliceous shales. The proportion of iron beds increases up-section (Fig. 5).

Section SW5a is located 600 m east of section SW5b and is exposed at the old mine site to the south of RW11 (Fig. 2). Based on geological mapping, strata from this section correlate with the strata in SW5b (Figs 2 and 5). A 5-m-thick diabase sill was identified in the southern part of this area, which is stratigraphically lower than the thick iron sequence. The lower iron sequence (1–4 m thick) comprises thinly laminated magnetite with silica laminae. The upper iron sequence (~8 m thick) is continuous and consists of laminated hematite interbedded with thin layers of red jasper nodules (Fig. 6A–B; sample 160320-06). The uppermost part of the iron sequence in SW5a comprises 3–8-cm-thick bedded magnetite layers (Fig. 6A and C; sample 160320-46).

Section SW5b is ca. 35 m thick and located ~80 m above the SW4 section. It is same stratigraphic level to SW5a and comprises greenish shale interbedded with a laminated iron sequence. A 2–3-m-thick iron bed in the lower part of the section forms an few meter scale isoclinal fold with the axial plane oriented parallel to bedding. This section overlies bedded volcaniclastic rocks. The iron sequence is interbedded with greenish siliceous shale and overlain by massive basaltic lava flows and a thick sequence of volcaniclastic rocks. This section contains a well-preserved contact between the iron sequence and overlying massive volcanic lava flows. Tight folding in the section might be related to bedding-parallel slip and flexural shearing of the beds by early thrusting. However, these displacements are not large and have not repeated the stratigraphy.

SW6, SW7a–b, and SW8 are thin iron sequences, which consist mainly of bedded magnetite. SW7b has been tightly folded, which might be related to thrusting. However, the stratigraphy of each of these sections has not been repeated. The stratigraphy in these sections only has estimated minimum thicknesses.

6. Optical microscopy and SEM observations

6.1 Methods

We examined rocks from the iron sequences and shales by scanning electron microscopy and energy dispersive X-ray spectrometry, along with electron backscatter diffraction imaging (FE-SEM; JSM-6500F at Kyushu University, Fukuoka, Japan). Each sample was prepared as a polished thin-section and observations were undertaken at a magnification of 1000–10,000×.

6.2 Results

Detailed petrographic observations of rock chips and thin-sections allowed three types of iron sequence rocks and greenish and black shales to be distinguished.

The massive magnetite-rich iron sequence is magnetite-rich, massive, homogeneous and contain 5–20-μm-sized euhedral cubic grains of magnetite disseminated within a quartz matrix (Figs 6C-1, C-2, C-3, and 7A-1, A2). The euhedral magnetite is unaltered and may have grown by hydrothermal or metamorphic processes.

The hematite-rich iron sequence is finely laminated, hematite-rich, banded on a scale of 2–5 cm, and contains thin nodular red jasper layers (0.5–1.0 cm thick; Figs 6D-1, D-2, D-3 and 7B-1, B-2). Microscopically, samples of the iron sequence contain: (1) ca. 10-μm -sized hematite grains surrounded by <3-μm -sized acicular hematite (Fig. 6D-3); (2) ca. 15-μm -sized euhedral magnetite grains, which are mostly martite formed from magnetite; (3) metamorphic amphibole and albite. Reddish brown parts of the iron beds are composed mostly of platy crystals of hematite (Fig. 6D-1). The thin nodular red jasper layers are mainly fine-grained quartz, along with some euhedral apatite and magnetite. The matrix comprises <30% of these beds and consists of jasper and clay minerals.

The graded magnetite-rich iron sequence is gradationally interbedded with well-laminated greenish and black shales (Fig. 4B–C). These iron sequence rocks are homogeneous and comprise silt-sized quartz grains set in a clay matrix (Fig. 7C). Euhedral magnetite that is <3 μm in size is preserved in a homogeneous clay-rich matrix (Fig. 7C) of fine-grained Al-rich minerals (e.g., clay), quartz, and organic matter.

The greenish and black shales exhibit well-preserved graded bedding and load cast structures (Fig. 4B–D). The greenish and black shales consist of primary plagioclase and amphibole, along with very fine-grained calcite, epidote, chlorite, sericite, and quartz (Fig. 7D-2 and E-2). Detrital fine sand- and silt-

sized quartz grains are well-preserved and comprise >40% of the matrix, which also contains <1-μm-sized organic matter and no iron oxides (Fig. 7D-2 and E-2).

7. Geochemistry

7.1 Methods

We undertook major and trace element, total organic carbon (TOC) content, and carbon isotopic analysis of the collected samples. The following three types of iron sequences and greenish shale samples were analyzed for major elements (Table 1): (1) massive magnetite-rich iron sequence (SW3a: 150321-08, 150321-11; SW5a: 150321-46, -46'; SW6a: 150322-06; SW7a: 160321-50; SE1: 150319-12; SE5: 150318-02); (2) hematite-rich iron sequence (SW4: 150321-22; SW5a: 150321-36, 37, 38, 39, 40, 42, 43, 44, 45); (3) graded magnetite-rich iron sequence (SW3a: 150321-07; 150321-07'; SW4: 150321-19). The 150321-07' data are for magnetite grains separated from sample 150321-07 from magnet separator. Some greenish shales were also analyzed (SW3a: 150321-09, SW5a: 160320-41, NE1: 160320-49).

Major element analyses were conducted on fused glass beads by wavelength-dispersive X-ray fluorescence spectrometry (WD-XRF; ZSX Promus II; Rigaku) at the National Museum of Nature and Science, Tsukuba, Japan.

The following three types of iron sequences and greenish shale samples were analyzed for trace elements (Table 3b): (1) massive magnetite-rich iron sequence (SW3a: 150321-08, 150321-11; SW5a: 150321-46'); (2) graded magnetite-rich iron sequences and shales (SW3a: 150321-07, 150321-07'; SW4: 150321-19); (3) hematite-rich iron sequence (SW4: 150321-22; SW5a: 150321-36) and three greenish shales (SW3a: 150321-09; SW5a: 160320-41; NE1: 160320-49).

Trace elements were analyzed in the same way as major elements. Rare earth elements (REEs) were analyzed by inductively coupled plasma mass spectrometry (Agilent Technologies 7500 Series ICP-MS) at the National Museum of Nature and Science, Tokyo, Japan. Two samples (15032-07' and 160320-46′) were prepared using a SELFRAG system that employs high-voltage pulse fragmentation to disaggregate samples at the National Polar Institute in Tokyo. The other samples were crushed to powder using a Multi-beads shocker® in a polycarbon sample holder at Kyushu University, Fukuoka, Japan.

REE data are plotted on Post-Archean Australian Shale (PAAS; Nance and Taylor, 1976; Taylor and MacLennan, 1985; Poumand et al., 2012)-normalized diagrams, because this normalization produced smoother heavy REE patterns than normalization to the North American Shale Composite (NASC). Y is also included in the REE diagrams, because Y is a REE with an ionic radius between that of Dy and Ho. The REE+Y diagram allows evaluation of the Y anomaly that can trace hydrothermal effects during iron deposition (e.g., Bau and Dulski, 1996; Zhang and Nozaki, 1996; Cox et al., 2013).

Organic carbon was separated from greenish and black shale samples. The powdered samples were decarbonated following the process described by Larson et al. (2008). Approximately 100 mg of each powdered sample was soaked in 6 N HCl for 3 d in an oven at 60˚C before analysis. The samples were

then rinsed in ultrapure water. All samples were enclosed in Sn cups for analysis. TOC and carbon isotope ($\delta^{13}C$) analysis were conducted by the combustion method using an elemental analyzer (Flash EA 1112) attached to a Thermo-Finnigan Delta Plus Advantage isotope ratio mass spectrometer at the Kochi core center of Kochi University, Kochi, Japan. Data calibration was carried out by analyzing two standards: L-alanine ($CH_3CH(COOH)NH_2$) obtained from the Sugito Laboratory for carbon isotopes; sulfanilamide ($C_6H_8N_2O_2S$) for TOC contents. These standards were analyzed before and after every 10 sample analyses. The uncertainty on the carbon isotope analyses is ±0.6‰ (1 SD of L-alanine analyses; n = 10). We analyzed fresh black shales from the SW4 section, which contains >7 m of black shale below the iron sequence and a 1-m-thick black shale within the iron sequence (Fig. 5).

7.2 Major and trace elements

Whole-rock major element data are listed in Table 1. Fe_2O_3 contents vary in the different iron sequence types. The massive magnetite-rich and graded magnetite-rich iron sequences contain 23–65 wt.% of Fe_2O_3 (average = 42.6 wt.%). The hematite-rich iron sequence samples have high Fe_2O_3 contents of 61–79 wt.% (average = 69.0 wt.%). The magnetite iron sequence (sample 160320-46) also has a high content of Fe_2O_3. Three iron sequence samples from El-Shazly et al. (2019) contained 41–53 wt.% of Fe_2O_3, which indicates these samples may be from the magnetite-rich iron sequence. The massive magnetite-rich and graded magnetite-rich iron sequences contain 23–65 wt.% of Fe_2O_3 (average = 42.6 wt.%). The hematite-rich iron sequence samples have high Fe_2O_3 contents of 61–79 wt.% (average = 69.0 wt.%).

SiO_2 contents negatively correlate with iron contents. The massive magnetite-rich and graded magnetite-rich iron sequences contain 22–45 wt.% of SiO_2 (average = 42.6 wt.%). The hematite-rich iron sequence samples have high SiO_2 contents of 12–30 wt.% (average = 69.0 wt.%). Al_2O_3 contents of the iron sequence samples are mostly 1.5–4.9 wt.%, and similar to those of other Rapitan-type BIFs (3.18 wt.%; Yeo, 1986). The graded magnetite-rich iron sequence in SW3b has high Al_2O_3 (7–11 wt.% Al_2O_3) and low iron contents (23–25 wt.% Fe_2O_3). Previously published iron sequence data also had high Al_2O_3 contents (2.6–7.3 wt.%; El-Shazly et al., 2019). The variable Al_2O_3 contents might be due to localized weathering. P_2O_5 contents vary from 0.6–2.6 wt.%, and are similar to analyses presented by El-Shazly et al. (2019).

The greenish shales located within the iron sequences (samples 150321-09 and 160321-41) and volcaniclastic rocks (sample 150321-49) have similar compositions. These shales have lower iron (4–7 wt.% Fe_2O_3) and phosphorus (ca. 0.1 wt.% P_2O_5) and higher aluminum (13–16 wt.% Al_2O_3) contents than the iron sequence samples. The high Al_2O_3 content is due to the clay minerals in the shales.

7.2 Trace and REE elements

PAAS-normalized REE patterns show enrichment in heavy REEs (Fig. 9; Table 2a and 2b). We add three iron samples data (Table 2c) from the El-Shazly et al. (2019) for comparison. All samples have

depleted light REE patterns. A small negative Eu anomaly characterizes sample 150321-08 from the massive magnetite-rich iron sequence. A small positive Eu anomaly characterizes the shale sample (150320-41) from within the volcaniclastic sequence in the NE domain. Sample 150321-07 from the graded magnetite-rich iron sequence has a very low total REE content. The shale and iron sequence samples have similar REE patterns and do not show a strong hydrothermal signature.

7.3 Total organic carbon contents and carbon isotopic data

TOC contents of the black shales (n = 9) in SW4 vary from 0.09 to 0.15 wt.%, and carbon isotope ($\delta^{13}C$) values range from −23.1‰ to −22.4‰ (Fig. 5; Table 3). The TOC contents are low, but the light carbon isotopic signatures suggest the carbon is potentially of biogenic origin. Detail discussion shows following chaper.

8. Depositional environment of the iron sequences

The source of iron and depositional environment are important factors in forming the iron sequences. The iron sequences in the CED have been suggested to have formed in an intra-back-arc setting (e.g., Ali et al., 2009; Basta et al., 2011; El-Shazly and Khalil, 2014; Khalil and El-Shazly, 2014; Khalil et al., 2015; Abd El-Rahman et al., 2019; El-Shazly et al., 2019). Based on the thick volcaniclastic sequence and island arc geochemical affinities it has been suggested that the El-Dabbah Group was deposited within the central rift zone of an immature island arc (Kiyokawa et al., in review), and in deeper water conditions than proposed by El-Shazly and Khalil (2016). The depositional places are expected near eruptive volcanos which produced the several thick accretionary lapilli tuff.

To identify the depositional environment, we considered: (1) the lithological and stratigraphic characteristics of the iron sequences; (2) continental input; (3) hydrothermal input; (4) Snowball Earth evidence; (5) oceanic redox conditions; and (6) biogenic activity.

8.1 Lithological and stratigraphic characteristics

In the El-Dabbah Group, the 2000-m-thick Middle El-Dabbah Formation contains seven iron-rich sequences (SW2 to SW8) within a sequence of volcanic lava flows and volcaniclastic rocks. Each iron sequence contains fine-grained greenish and black shales, which may be tuffs, hemipelagic shales, and precipitated organic matter. The three types of iron sequence indicate that iron sedimentation varied in terms of the amount and rate of iron deposition. Graded beds are suggestive of a reduced volcanic tuff input or increasing iron deposition. In a volcanic tuff, the iron content is not high, and so increased iron precipitation may have been responsible for reducing volcanic eruption to change quiescence period.

The hematite-rich iron sequence near the iron mine site in the El-Dabbah Group does not preserve original sedimentary textures and structures. Magnetite has been transformed to hematite and jasper

nodule layers have formed. The massive magnetite-rich iron sequence rocks contain magnetite set in a silicate matrix. Martite formed as hematite pseudomorphs after magnetite, which probably occurred during weathering or late-stage hydrothermal alteration. The graded magnetite-rich iron sequence contains primary sedimentary structures and, in particular, graded bedding marked by an upward increase in disseminated iron within the greenish and black shales.

Sedimentary structures, such as parallel laminations, load casts, and graded beds, are well-preserved in each greenish shale, black shale and iron beds. However, these sedimentary sequences do not contain coarse detrital volcaniclastic grains and cross-bedded sandy sequences. Above and below of these shale and iron sequence also have less vesicular pillow basalts and accretional lapilli. These lines of evidence suggest that sedimentation occurred in a low-energy and relatively deep environment. Sedimentation of the iron sequences may have occurred during periods of quiescence between oceanic island volcanic activity. Modern example of oxyhydroxide sedimentation in ocean have very first precipitation, such as 30 cm/year in the Satsuma Iwo Jima island (Kiyokawa and Ueshiba, 2015). In the way, quiescence time for iron deposition may not spent long period.

8.2 Continental input

Based on detailed thin-section observations, continental-derived quartz and other clastic materials are not present in the studied samples. This is consistent with the low Al, Ti, K, and Na contents. Only the graded magnetite-rich iron sequence has relatively high contents of these elements, which may be related a shale component (Table 1).

The Al/(Al+Fe+Mn+Na+K+Ca) ratio can be used to identify the depositional environment (Bostrom, 1970; Peter, 2003; Cox et al., 2013; Abd El-Rahman et al., 2019). Our data suggest the shales are volcanogenic sediments, but most of the iron sequence samples are hydrothermal sediments or a mixture of these and volcanogenic sediments (Fig. 9). No samples are detrital continental terrigenous sediments.

8.3 Evidence for hydrothermal activity

Eu and Y anomalies and Y/Ho ratios are commonly used to identify hydrothermal activity (e.g., Klinkhammer et al., 1994; Bau et al., 1996; Douville et al., 1999). Eu anomalies record the hydrothermal fluids formed during high pressure/temperature alteration of oceanic crust, which is dominated by crystal chemical exchange with plagioclase (especially albite) (Blundy and Wood, 1991). Hydrothermal fluids lead to positive Eu anomalies in sediments. Y is geochemically similar to the REEs, and especially Ho (Jochum et al., 1986; Govindaraju, 1989). High Y/Ho ratios in some fluids can be due to mixing of hydrothermal fluids with seawater during REE scavenging by iron (oxy)hydroxides (Bau et al., 1996; Bau and Dulski, 1999).

REE data for the El-Dabbah Group exhibit negative Eu anomalies (Eu/Eu* = 0.28–0.88), no Ce anomalies (Ce/Ce* = 0.94–1.05), and slight heavy REE enrichment. The REE patterns of the iron

sequence samples are similar to those of the shales within the volcaniclastic sequence. This suggests that iron was not directly sourced from high-temperature hydrothermal fluids, but may have been related to low-temperature fluids or even a setting devoid of hydrothermal activity.

Y/Ho ratios in the studied sediments are 23.85–34.25, which are superchondritic (Y/Ho > 27.7), and similar to those of most NIFs (mean Y/Ho = 29.2; n = 77: Cox et al., 2013). This also does not suggest there was a high temperature hydrothermal input.

Basta et al. (2011) showed that iron sequences from Wadi Kareim (50 km north of Wadi El-Dabbah) and Um Anab (100 km north of Wadi El-Dabbah; upper greenschist-facies rocks) also lack positive Eu anomalies (Abd El-Rahman et al., 2019). These patterns are not typical of Archean Algoma-type iron sequences, which always exhibit a positive Eu anomaly due to their high-temperature hydrothermal origin (e.g., Klein and Beukes, 1993). In addition, REE patterns of the iron sequences from Hadrabia, Um Shaddad, and Um Ghamis are variable due to weathering effects, but unaltered iron sequences from Hadeed, El-Dabbah, Um Nar, Gebel El Hadid, and Wadi Kareim are slightly enriched in heavy REEs (El-Shazly and Khalil, 2014; Khalil et al., 2015; Abd El-Rhaman et al., 2019). These iron sequences have similar REE features to our data.

In addition, most of the iron beds do not directly overlie lava flows, but always occur within fine-grained greenish and black shales. The field observations and geochemical signatures suggest that iron sedimentation occurred at low temperatures during times of volcanic quiescence under ambient seawater conditions.

8.4 Redox conditions

Redox conditions are also important for identifying the depositional environment of iron sedimentation, as this requires oxic conditions. The paleo-redox conditions were evaluated with Ni/Co, V/Cr, and V/(V+Ni) ratios (Jones and Manning, 1994; Rimmer, 2004), U/Th and Cu/Zn ratios (Jones and Manning, 1994), and Ce anomalies. Ce is sensitive to variations in the redox condition and $Ce_{(N)}/Ce^*$ ratios ($Ce^* = \sqrt{(La_{(N)} + Pr_{(N)})}$; (N = normalized to PAAS) of >0.10 reflect oxic conditions and <0.10 reflect anoxic conditions (Wilde et al., 1996; Yang, 2011).

V/(V+Ni) ratios of >0.84 suggest euxinic conditions, 0.54–0.82 represent anoxic conditions, and 0.46–0.60 represent dysoxic conditions (Rimmer, 2004). In the present study, Ni/Co ratios indicate oxic to dysoxic conditions (Fig. 10), whereas V/(V+Ni) ratios indicate anoxic to euxinic conditions (Fig. 10).

U/Th ratios of >1.25 indicate anoxic conditions (Nath et al., 1997). In this study, U/Th ratios vary from 1.9–8.5, which are suggestive of anoxic conditions. High Cu/Zn ratios indicate reducing conditions, whereas low Cu/Zn ratios indicate oxidizing conditions (Hallberg, 1976). Our Cu/Zn ratios vary from 0.06–0.87, but the massive magnetite-rich iron sequence sample 150321-11 has a high ratio (8.00). Ce/Ce* values of 0.96–1.05 are also inconsistent with oxic conditions.

These geochemical proxies suggest the sedimentary environment in the El-Dabbah Group was mostly anoxic, but occasionally oxic to dysoxic. We identfied the sedimentation basin condition might be situated mostly oxic and locally preserved redox boundary condition such as narrow deep oceanic basins.

8.5 Biogenic activity

The black shales have a narrow range of $\delta^{13}C$ values from ca. –22‰ to –23‰, consistent with a cyanobacterial origin (Schidlowski, 1998) prior to oxic iron sedimentation. These values are lighter than those of Archean black shales (33‰–28‰; e.g., Kiyokawa et al., 2006, 2012, 2014). Low TOC contents (ca. 0.1 wt.%) might be due to mixing with fine-grained volcanogenic sediment. TOC contents of the black shales provide further evidence for bottom water anoxia. The greenish and black shales beneath many of the iron sequences indicate that biogenic material was precipitated from the near-surface ocean to the ocean floor prior to iron sedimentation. The black shales reflect anoxic conditions at the seafloor, which preserved the organic matter. The greenish shales are mainly fine tuffs and hemipelagic shales, which may have been deposited in oxic–dysoxic conditions.

Iron oxidation at the sea surface caused by cyanobacterial blooming may have led to rapid iron sedimentation in anoxic bottom waters. The light carbon isotopes of the black shales were likely inherited from the cyanobacteria.

8.6 Sedimentary environment

In the study area, the iron sequences always overlie fine-grained, greenish, siliceous shales and black shales. No iron sequences directly overlie massive lava flows. The iron sequences are distributed over an area that is several kilometers across. Geochemical data indicate a low-temperature hydrothermal origin or no hydrothermal input. As such, we suggest that iron sedimentation in the El-Dabbah Group occurred during periods of volcanic quiescence throughout the formation of the 7000-m-thick volcaniclastic sequence. Iron sedimentation may have occurred in a small basin in the central rift zone of an immature island arc (El-Shazly and Khalil, 2014; Kiyokawa et al., in review).

The multiple iron sequences of different thicknesses do not imply periodic deposition. The iron sequences were deposited irregularly during non-volcanic periods. In particular, the Middle El-Dabbah Formation preserves numerous iron sequences, and shows no evidence of glaciation such as diamictites and dropstones, but instead contains tuffs, organic-rich shales, and iron sequences. In this area, the ocean floor was not covered by sediment from ice sheets and icebergs.

REE data show that the iron sequences were not directly associated with high-temperature hydrothermal fluids, similar to other NIFs (e.g., Klein and Ladeira, 2004; Cox et al., 2013). Most iron sequences in Egypt are similar to Algoma-type BIFs (e.g., Khalil et al., 2015), and have been linked to arc volcanism. But most NIFs were deposited under low-temperature hydrothermal conditions or were

unrelated to hydrothermal activity (Besta et al., 2011; Stern et al., 2013). Low-temperature waters can contain dissolved Fe^{2+}. Based on the sedimentary depositional environment, the iron source was probably low-temperature hydrothermal fluids associated with the rifted island arc setting.

However, continental break-up, such as the rifting of Rodinia, and subduction volcanism during this time may have increased the iron content of seawater (e.g., Hoffman and Schrag, 2002, Hoffman et al., 2017). The superchondritic Y/Ho ratios of the iron sequences, however, preclude a continental input and continental rift setting.

The evidence for cyanobacteria in the El-Dabbah Group means that iron oxidation was likely triggered just prior to iron precipitation. If iron was already saturated in the ocean and a cyanobacterial bloom occurred around an island arc, then iron deposition would have occurred.

The reported ages of the iron sequences are variable. Most probable sedimentation ages from Gebel El Hadid of 717 ± 8 Ma (Khalil et al., 2015) and Wadi Hamama of 696–693 Ma (Abd El-Rhaman et al., 2019). NIFs in the CED may have formed throughout the Sturtian and not just after one Snowball event (Rooney et al., 2015; Abd El-Rhaman et al., 2019). Variable slightly different sedimentation NIF ages support their formation may be deposited in small basins in different time island arc activities.

The tectonic setting of the CED from 800–700 Ma was at the western edge of the Rodinia supercontinent (Li et al., 2008). This suggests the immature island arc was formed near the western part of Rodinia external super ocean (Mirovoi Ocean). The El-Dabbah Group contains fine-grained sediments that might have been deposited in an open ocean environment. We suggest the El-Dabbah Group was deposited in a small basin in the central rift zone of an immature island arc (Fig. 11).

Modern glacial settings contain ice-rafted debris (IRD) that originates from continental ice sheets that melt along continental margins (e.g., Rydningenab et al., 2013). It is difficult to form IRD deposits in isolated oceanic island arc settings. If sedimentation of the El-Dabbah Group coincided with a Snowball Earth event, and thus occurred beneath sea ice, oxidation might have occurred during the opening of sea ice due to periodic volcanic eruptions and emanating hot springs (Fig. 9). The following well-known scenario describes how iron sequences are deposited during recovery from a Snowball Earth event (e.g., Hoffman and Schrag, 2002; Hoffman and Li, 2009; Hoffman et al., 2011). Once the sea surface is covered with ice, there is little or no exchange between the sea and atmosphere. Hydrothermal activity could, however, still continue to produce CO_2 and iron (Fe^{2+}). An active oceanic arc volcano might have melted some ice. The open ocean would have led to biological activity that produced oxygen and organic matter (e.g., cyanobacteria) that would have been deposited as black shales on the anoxic ocean floor. The greenish shales were deposited fine distal tuff from the volcano and from coated ice surface. The cyanobacterial activity produced oxygen and dissolved Fe^{2+} was then oxidized and precipitated as Fe^{3+} in the ocean during periods of volcanic quiescence.

In such a scenario, the sea ice surrounding the island arc would not generate dropstones, diamictites, IRD, or debris flows. However, volcanic tuffs, which covered sea ice around oceanic island arc, might be

deposition after melting ice seat as hemipelagic shale. In this case, several greenish shales might have been related to glaciation. Ali et al. (2010) reported diamictite sections near the iron sequences at Wadi Kareim. This might represent evidence of glaciation. If deposition of the El-Dabbah Group was rapid, then evidence of glaciation would be present above and below the El-Dabbah Group. In addition, the muddy matrix-supported debris flow conglomerate (resembling a diamictite) preserved in the Atshan Formation (Kiyokawa et al., in review). The Atshan Formation might be related glaciation event. But detail stratigraphy and deposition age of the Atshan Formation are still not well known.

As such, the relationship between iron sedimentation in the El-Dabbah Group and the Snowball Earth model remains unclear. Detailed mapping, stratigraphic reconstructions, and high-quality age constraints for the NIFs in the CED might lead to a better understanding of this relationship.

9. Conclusions

1) At least nine iron sequences were documented in a 5500-m-thick volcaniclastic sequence of the El-Dabbah Group. This group comprises the Lower El-Dabbah Formation (massive volcanic rocks, such as microgabbro, massive lava, pillow lava and miner volcaniclastic rock with thin iron sequence), Middle El-Dabbah Formation (pillow lavas, volcaniclastic rocks, accretionary lapilli tuff layers, greenish-black shales and iron sequences), and Upper El-Dabbah Formation (relatively shallow volcaniclastic sequence with pillow lava, volcaniclastics and greenish shales).
2) Low Al, Ti, K, and Na contents and Al/(Al+Fe+Mn+Na+K+Ca) ratios suggest there was no continental input. REE data lack Eu and Ce anomalies and exhibit enrichment in heavy REEs, similar to the greenish and black shales within the iron sequences and surrounding volcaniclastic rocks. This suggests the iron sequences record a low-temperature hydrothermal fluid signature of a central rift zone of oceanic island arc.
3) Black shales in the volcaniclastic and iron sequences have very low TOC contents and light $\delta^{13}C$ values of –22‰ to –23‰, suggesting a cyanobacterial origin. Cyanobacterial activity may have occurred during periods of volcanic quiescence. The ocean bottom waters were relatively reducing, which facilitated the preservation of organic matter in black shale.
4) Lithological and geochemical evidence suggest a non-continental source and low-temperature hydrothermal origin for the iron sequences in the El-Dabbah Group. The depositional environment was an isolated oceanic island arc setting. Iron deposition occurred in a small rift-related basin near an island arc.
5) There is no evidence for glaciation in the El-Dabbah Group. However, the stratigraphy and geochemical data are not inconsistent with Snowball Earth conditions during the Sturtian.

Acknowledgements

We thank Takashi Sano and Yukiyasu Tsutsumi of the National Science Museum of Tokyo for their assistance with REE and XRF analyses. This study was supported by Grants-in-Aid from the Japanese Ministry of Education, Culture, Sports, Science, and Technology (22253008 and 26257211). We acknowledge the assistance of the 2016 short-time research dispatch–invite program of Kyushu University and the Kochi Core Center. This study was undertaken with the cooperation of the Center for Advanced Marine Core Research (CMCR) of Kochi University (13A002, 13B002, 14A009, 14B007, 15A050, 15A045, 16A038, 16B034, 17A002, and 17B002) and Menoufiya University.

References

Abd El-Rahman Y., Polat A., Dilek Y., Kusky T.M., El-Sharkawi M., Said A., 2012. Cryogenian ophiolite tectonics and metallogeny of the Central Eastern Desert of Egypt. International Geology Review, 54, 16, 1870–1884.

Abd El-Rahman, Y., Gutzmer, J., Li, X.H., Seifert T., Li, C.F., Ling, X.X., Li, J., 2019. Not all Neoproterozoic iron formations are glaciogenic: Sturtian-aged non-Rapitan exhalative iron formations from the Arabian–Nubian Shield. Mineralium Deposita. 1-20, Online. https://doi.org/10.1007/s00126-019-00898-0

Ali, K.A., Stern, R.J., Manton, W.I., Kimura, J.-I., Khamees, H.A., 2009. Geochemistry, Nd isotopes and U-Pb SHRIMP zircon dating of Neoproterozoic volcanic rocks from the Central Eastern Desert of Egypt: new insights into the ~750 Ma crust-forming event. Precambrian Research, 171, 1–22.

Ali, K.A., Stern, R.J., Manton, W.I., Johnson, P.R., Mukherjee, S.K., 2010. The Neo-proterozoic Atud Diamictite of the Eastern Desert of Egypt and Northern Saudi Arabia: evidence of ∼750 Ma glaciation in the Arabian-Nubian Shield? International Journal of Earth Sciences 99, 705–726.

Basta, F.F., Takla, M.A., Maurice, A.E., 2000. The Abu Marawat BIF: geology, mineralogy, geochemistry and origin. The 5th International Conference on the Geology of the Arab World, Cairo University, pp. 319–334.

Basta, F.F., Maurice, A.E., Fontbote L., Favarger P.Y., 2011. Petrology and geochemistry of the BIF (BIF) of Wadi Karim and Um Anab, Eastern Desert, Egypt: Implications for the origin of Neoproterozoic BIF. Precambrian Research, 187, 277–292.

Bau, M. and Dulski, P., 1996. Distribution of yttrium and rare-earth elements in the Penge and Kuruman iron-formations, Transvaal Supergroup, South Africa. Precambrian Research. 79, 1-2, 37-55.

Bau, M. and Dulski, P., 1999. Comparing yttrium and rare earths in hydrothermal fluids from the Mid-Atlantic Ridge: implications for Y and REE behavior during near-vent mixing and for the YrHo ratio of Proterozoic seawater. Chemical Geology, 155, 77-90.

Bau, M., Koschinsky, A., Dulski, P., Hein, J.R., 1996. Comparison of the partitioning behaviours of yttrium, rare earth elements, and titaniumbetween hydrogeneticmarine ferromanganese crusts and seawater. Geochimica et Cosmochimica Acta, 60, 10, 1709–1725.

Bekker, A., Holland, H.D., Wang, P. L., Rumble, D., Stein, H.J., Hannah, J.L., Coetzee, L.L., Beukes, N.J., 2004. Dating the rise of atmospheric oxygen. Nature, 427, 117─120.

Bekker, A., Kaufman, A.J., 2007. Oxidative forcing of global climate change: A biogeochemical record across the oldest Paleoproterozoic ice age in North America: Earth and Planetary Science Letters, 258, 486─499.

Bostrom, K., 1970. Submarine volcanism as a source for iron. Earth Planetary Science Letter. 9, 4, 348–354.

Blundy J.D. and Wood, B.J., 1991. Crystal-chemical controls on the partitioning of Sr and Ba between plagioclase feldspar, silicate melts, and hydrothermal solutions. Geochimica et Cosmochimica Acta, 55, 193-209.

Cribb, J.W., Barton, M., 1996. Geochemical effects of decoupled fractional crystallization and crustal assimilation. Lithos, 37, 4, 293–307.

Cox, G.M., Halverson G.P., Minarik W.G., Le Heron D.P., Macdonald F.A., Bellefroid E.J., Strauss J.V., 2013. Neoproterozoic iron formation: An evaluation of its temporal, environmental and tectonic significance. Chemical Geology, 362, 232-249.

Douville, E., et al., 1999. Yttrium and rare earth elements in fluids from various deep-sea hydrothermal systems. Geochimica et Cosmochimica Acta, 63, 5, 627–643.

EGSMA (Egyptian Geological Survey and Mining Authority), 1996. Geological map of Wadi Jabjahah Quadrangle, Egypt, Scale 1:250.000. Egyptian Geological Survey and Mining Authority, Cairo, Egypt

EGSMA (Egyptian Geological Survey and Mining Authority), 2002. Geological Map of Marsa Shaab Quadrangle, Egypt at Scale 1:250,000. Egyptian Geological Survey and Mining Authority, Cairo, Egypt

El-Habaak, G.H., 2004. Pan-African skarn deposits related to BIF, Um Nar area, central Eastern Desert, Egypt. Journal of African Earth Sciences, 38, 2, 199-221.

El-Habaak, G.H., Soliman, M.F., 1999. Rare earth elements geochemistry of the Egyptian BIFs and the evolution of the Precambrian atmosphere and ocean. 4th International Conference on Geochemistry, Alexandria University, Egypt. pp. 149–169.

El-Shazly A.K. and Khalil K.I., 2014. BIFs of Um Nar, Eastern Desert of Egypt: P-T-X conditions of metamorphism and tectonic implications. Lithos, 196-197, 356-375.

El-Shazly A.K. and Khalil K.I., 2016. Metamprphic and geochronologic constraints on the tectonic evolution of the Central Eastern Desert of Egypt. Precambrian Research, 283, 144-168.

El-Shazly A.K., Khalil K.I., Helba H.A., 2019. Geochemistry of banded iron formations and their host rocks from the Central Eastern Desert of Egypt: A working genetic model and tectonic implication. Precambrian Research, 325, 192-216.

Eyles, N. and Januszczak N., 2004. 'Zipper-rift': a tectonic model for Neoproterozoic glaciations during the breakup of Rodinia after 750 Ma. Earth Science Reviews, 65, 1-2, 1-73.

Fowler, A.R., Hamimi, Z., 2019. Structural and Tectonic Frame work of Neoproterozoic Basement of Egypt: From Gneiss Dome to Transpression Belts. In: Hamimi Z., El-Barkooky A., Frias J.M., Fritz H., El-Rahman A.E., (Eds), The geology of Egypt, 82-129, Springer Nature, Switzerland.

Fritz H., Messner M., 1999. Intramontane basin formation during oblique convergence in the Eastern Desert of Egypt: magmatically versus tectonically induced subsidence. Tectonophysics, 315, 145-162.

Gaucher C., Sial A.N., Frei, R. 2015. Chapter 17 - Chemostratigraphy of Neoproterozoic Banded Iron Formation (BIF): Types, Age and Origin. (Eds.) M. Ramkumar, Chemostratigraphy, Concepts, Techniques, and Applications., 433-449. Elsevire, Amsterdam.

Gross, G.A., 1980. A classification of iron-formation based on depositional environments. Canadian Mineralogist, 18, 215–222.

Govindaraju K., 1989, 1989 compilation of working values and sample description for 272 geostandards. Geostandards Newsletter 13, 1–113.

Hallberg, R.O., 1976. A Geochemical Method for Investigation of Palaeoredox Conditions in Sediments. Ambio Special Report, 4, 139-147.

Hoffman, P.F., Kaufman, A.J., Halverson, G.P., Schrag, D.P., 1998. A Neoproterozoic snowball Earth. Science, 281, 1342–1346.

Hoffman, P.F. and Schrag, D.P., 2002. The snowball Earth hypothesis: testing the limits of global change. Terra Nova 14, 129–155.

Hoffman, P.F., Dorian, S. Abbot, D.S., Ashkenazy, Y., Benn, D.I., Brocks, J.J., Cohen, P.A., Cox, G.M., Creveling, J.R., Donnadieu, Y., Erwin, D.H., Fairchild, I.J., Ferreira, D., Goodman, J.C., Halverson, G.P., Jansen, M.F., Le Hir, G., Love G.D., Macdonald F.A., Maloof, A.C., Partin C.A., Ramstein G., Rose B.E. J., Rose, C.V., Sadler P.M., Tziperman, E., Voigt, A., Warren S.G. 2017. Snowball Earth climate dynamics and Cryogenian geology-geobiology. Science Advances, 3: 1-43, e1600983

Hoffman, P.F. and Li, Z.X., 2009. A Palaeogeographical context for Neoproterozoic glaciations. Palaeogeography, Palaeoclimatology, Palaeoecology, 277, 158–172.

Hoffman, P.F., Macdonald F.A., Halverson G.P., 2011. Chemical sediments associated with Neoproterozoic glaciation: iron formation, cap carbonate, barite and phosphorite. In: Arnaud A.E., G.P., Halverson, Shields-Zhou G., (eds) The Geological Record of Neoproterozoic Glaciations. Geological Society, London Memoirs, 36, 67–80.

Holland, H.D., 1983. The Chemical Evolution of the Atmosphere and Oceans. Princeton University Press, Princeton, 582p.

Isley, A.E., Abbott, D.H., 1999. Plume-related mafic volcanism and the deposition of banded iron formation. Journal of Geophysical Research. 104, 15461–15477.

James, H.L.,1983. Distribution of BIF in space and time, in: Trendall, A.F., and Morris, R.C., Eds, Iron-formation: Facts and Problems: Amsterdam, Elsevier, p. 471–490.

Jochum K. P., Seufert H. M., Spettel B., and Palme H., 1986. The solar-system abundances of Nb, Ta, Y, and the relative abundances of refractory lithophile elements in differentiated planetary bodies. Geochimica Cosmochimica Acta, 50, 1173–1183.

Johnson, P.R., Andresen A., Collins A.S., Fowler A.R., Fritz H., Ghebreab W., Kusky T., Stern R.J., 2011. Late Cryogenian-Ediacaran history of the Arabian-Nubian Shield: A review of depositional,

plutonic, structural, and tectonic events in the closing stages of the northern East African Orogen. Journal of African Earth Sciences, 61, 167–232.

Jones B. and Manning D.C., 1994. Comparison of geochemical indices used for the interpretation of paleo-redox conditions in Ancient mudstones. Chemical Geology, 111, 1-4, 111-129.

Khalil, K.I. and El-Shazly, A.K., 2014. Petrological and geochemical characteristics of Egyptian BIFs: review and new data from wadi Kareim. Geochem. Explor. Environ. Anal. 12, 105-126.

Khalil K.I., El-Shazly A.E., Lehmann B., 2015. Late Neoproterozoic BIF (BIF) in the central Eastern Desert of Egypt: Mineralogical and geochemical implications for the origin of the Gebel El Hadid iron ore deposit. Ore Geology Reviews, 69, 380-399.

Kirschivink, J.L. (Ed.), 1992. Late Proterozoic Low-Latitude Global Glaciation: the Snowball Earth. The Proterozoic Biosphere: a Multidisciplinary Study. Cambridge University, Press, New York.

Kiyokawa S., Ito T., Ikehara M. and Kitajima F., 2006. Middle Archean volcano-hydrothermal sequence: bacterial microfossil- bearing 3.2-Ga Dixon Island Formation, coastal Pilbara terrane, Australia. Geological Society of America Bulletin, vol. 118, no. 1/2, 3-22.

Kiyokawa S., Ito, T., Ikehara, M., Yamaguchi, K.E., Koge S. and Sakamoto, R., 2012. Lateral variations in the lithology and organic chemistry of a black shale sequence on the Mesoarchean sea floor affected by hydrothermal processes: the Dixon Island Formation of the coastal Pilbara Terrane, Western Australia. The Island Arc. v.21, 2, 66-78.

Kiyokawa S., Koge S., Ito T., Ikehara M., 2014. An ocean-floor carbonaceous sedimentary sequence in the 3.2-Ga Dixon Island Formation, coastal Pilbara terrane, Western Australia. Precambrian Research, 255, 124-143.

Kiyokawa S. and Ueshiba T., 2015. Rapid sedimentation of iron oxyhydroxides in an active hydrothermal shallow semi-enclosed bay at Satsuma Iwo-Jima Island, Kagoshima, Japan. Sedimentary Geology, 319, 98-113.

Klein, C., 2005. Some Precambrian banded iron-formations (BIFs) from around the world: Their age, geologic setting, mineralogy, metamorphism, geochemistry, and origins. American Mineralogist. 90, 10, 1473–1499.

Klein, C., Beukes, H.J., 1993. Sedimentology and geochemistry of the glacigenic Late Proterozoic Rapitan iron-formation in Canada. Economic Geology, 88, 542–565.

Klein, C., Ladeira, E.A., 2004. Geochemistry and mineralogy of Neoproterozoic BIFs and some selected, siliceous manganese formations from the Urucum District, Mato Grosso do Sul, Brazil. Economic Geology, 99, 1233–1244.

Klinkhammer, G.P., Elderfield, H., Edmond, J.M., Mitra, A., 1994. Geochemical implications of rare earth element patterns in hydrothermal fluids from mid-ocean ridges. Geochimica et Cosmochimica Acta, 58, 23, 5105–5113.

Larson, T.E., Heikoop J.M., Perkins G., Chipera, S.J., Hess, M.A. 2008. Pretreatment technique for siderite removal for organic carbon isotope and C:N ratio analysis in geological samples. Rapid Communications in Mass Spectrometry, 22, 865-872.

Li, Z.X., Bogdanova, S.V., Collins, A.S., Davidson, A., De Waele, B., Ernst, R.E., Fitzsimons, I.C.W., Fuck, R.A., Gladkochub, D.P., Jacobs, J., Karlstrom, K.E., Lu, S., Natapov, L.M., Pease, V., Pisarevsky, S.A., Thrane, K., Vernikovsky, V., 2008. Assembly, configuration, and break-up history of Rodinia: a synthesis. Precambrian Research. 160, 179–210.

Mamimi, Z., Abd El-Wahed M.A., Gahlan H.A., Kamh S.Z., 2019. Tectonics of the Eastern Desert of Egypt; Key to understanding the Neoproterozoic evolution of the Arabian-Nubian Shield (East African Orogen). A. Bendaoud et al. (eds.), The Geology of the Arab World—An Overview, 1-80, Springer Nature Switzerland.

Marchig, V., Gundlach, H., 1982. Iron-rich metalliferous sediments on the East Pacific Rise: prototype of undifferentiated metalliferous sediments on divergent plate boundaries. Earth Planetary Science Letter, 58, 3, 361–382.

Nance, W.B., Taylor, S.R., 1976. Rare earth element patterns and crustal evolution-I. Australian post-Archean sedimentary rocks. Geochimica et Cosmochimica Acta, 40, 1539-1551.

Nath B.N., Bau M., Ramalingeswara Rao B., Rao ChM., 1997. Trace and rare earth elemental variation in Arabian Sea sediments through a transect across the oxygen minimum zone. Geochimica et Cosmochimica Acta, 61, 12, 2375-2388..

Peter J.M., 2003. Ancient iron formations: their genesis and use in the exploration for stratiform base metal sulfide deposits, with examples fromthe Bathurst Mining Camp. In: Lentz D.R. Ed., Geochemistry of sediments and sedimentary rocks: evolution considerations to mineral deposit-forming environments, vol 4. Geological Association of Canada, GeoText, pp 145–176

Pourmand A., Dauphas N., Ireland T.J., 2012. A novel extraction chromatography and MC-ICP-MS technique for rapid analysis of REE, Sc and Y: Revising Cl-chondrite and Post-Archean Australian Shale (PAAS) aboundances. Chemical Geology, 291, 38-54.

Rimmer S.M., 2004. Geochemical paleoredox indicators in Devonian-Mississippian black shales, Central Appalachian Basin (USA). Chemical Geology, 206, 373–391.

Rooney, A. D., Struss J.V., Brandon A. D., Macdonald F. A., 2015. A Cryogenian chronology: Two long-lasting synchronous Neoproterozoic glaciations. Geology, 43, 459–462.

Rydningenab A.T., Vorren T.O., Laberg J.S., Kolstad V., The marine-based NW Fennoscandian ice sheet: glacial and deglacial dynamics as reconstructed from submarine landforms. Quaternary Science Reviews, 68, 15, 126-141.

Schidlowski, M., 1988. A 3,800-million-year isotopic record of life from carbon in sedimentary rocks. Nature, 333, 313-318.

Sims, P.K. and James, H.L., 1984. BIFs of late Proterozoic Age in the Central Eastern Desert of Egypt: geology and tectonic setting. Economic Geology, 79, 1777–1784.

Stern, R. J. and Hedge, C. E., 1985. Geochronologic and isotopic constraints on late Precambrian crustal evolution in the Eastern Desert of Egypt. American Journal of Science, 285, 2, 97-127.

Stern, R.J., Mukherjee, S.K., Miller, N.R., Ali, K., Johnson, P.R., 2013. ~750 Ma BIF from the Arabian-Nubian Shield—Implications for understanding neoproterozoic tectonics, volcanism, and climate change. Precambrian Research, 239, 79– 94.

Taylor, S.R., McLennan, S.M., McCulloch, M.T., 1983. Geochemistry of loess, continental crustal composition and crustal model ages. Geochimca et Cosmochimic Acta, 47, 11, 1897–1905.

Taylor, S.R., McLennan, S., 1985. The Continental Crust: Its Composition and Evolution. Blackwell Scientific Publications. 312 pp.

Wilde P., Quinby M.S., Erdtmann B.D., 1996. The whole-rock cerium anomaly: a potential indicator of eustatic sea-level changes in shales of anoxic facies. Sedimentary Geology, 10, 43.

Yang B., Hu B., Bao Z., Zhang Z., 2011. REE geochemical characteristics and depositional environment of the black shale-hosted Baiguoyuan Ag-V deposit in Xingshan, Hubei Province, China. Journal Rare Earths. 29, 5, 499.

Young, G.M., 1976. Iron formation and glaciogenic rocks of the Rapitan Group, Northwest Territories, Canada. Precambrian Research, 3, 137─158.

Yeo, G.M., 1986. Iron-formation in the Late Proterozoic Rapitian Group, Yukon and Northwest Territories. In: Morin, J.A. (ed.) Mineral Deposists of the Northern Cordillera. Canadian Institute of Mineralogy and Metallurgy Special Volume, 37, 142-153.

Zhang, J. and Nozaki, Y., 1996. Rare earth elements and yttrium in seawater: ICP-MS determinations in the East Caroline, Coral Sea, and South Fiji basins of the western South Pacific Ocean. Geochimica et Cosmochimica Acta, 60, 23, 4631-6444.

Figures

Fig. 1. Map of the Arabian–Nubian Shield and distribution of BIFs in the CED, Egypt (after Basta et al., 2011). The point labeled “7” is the Wadi El-Dabbah area shown in detail in Fig. 2. The geological map was modified after Geological Survey of Egypt (EGSMA) 1:250,000 Geological Map series (1996, 2002), Jonson et al. (2011) and Kiyokawa et al., (in review). The tectonic map was modified after Jonson et al. (2011) and overlain on a Google Earth image. The BIF locations are as follows: 1 = Um Anab; 2 = Hadrabia; 3 = Abu Marawat; 4 = Semna; 5 = Abu Diwan; 6 = Wadi Kareim; 7 = Wadi El-Dabbah; 8 = Um Shaddad; 9 = Um Ghamis El Zarqa; 10 = Gebel El Hadid; 11 = El Emra; 12 = Um Nar; 13 = Wadi Hammama.

Fig. 2. Geological map of the Wadi El-Dabbah area superimposed on Google Earth imagery. At right is a N–S cross-section of the NW and SW tectonic domains. RW and RE indicate the various dry gorge names (e.g., RW12) mentioned in the text. Red characters indicate the locations of measured sections (after Kiyokawa et al., in review).

Fig. 3. (left) Composite stratigraphy of the Wadi El-Dabbah area (after Kiyokawa et al., in review). (right) Detailed stratigraphy of the iron-rich part of the Middle El-Dabbah Formation in the SW domain. SW1 to SW7 and NW1 are the IF sequence locations. Detail SW1, SW3, SW4 and SW5 stratigraphic columns shown in Fig. 4.

Fig. 4. (A) Field photographs of measured sections SW4 and SW5b in the upper area of RW12. Black-colored layers are the massive magnetite-rich iron sequences. View to the west from entrance of RW12. (B) Massive magnetite-rich iron sequence overlying greenish siliceous shales at the top of section SW3a (sample 150321-11). (C) Hematite-rich iron sequence at the top of SW4 (sample 150321-22). Fining- and thinning-upward, greenish, siliceous shale beds gradually transition to iron beds. (D) Well-laminated black shale and fine-grained volcanogenic sediment. Finely and wavy laminated (with load casts) greenish and black shale succession in SW4. (E) Black shale in SW4 (sample 20150321-15) consisting mainly of silt-sized quartz, plagioclase, and organic matter.

Fig. 5. Detailed stratigraphic columns of the iron-rich strata. Column locations are as follows: SW1 at RW13; SW3a to SW5b at RW12; SW5a on the western side of the main wadi south of RW11 near the old iron mine (Figs 2–3). Total organic carbon (TOC) and carbon isotopic ($\delta^{13}C_{org}$) data for the black shales are shown alongside SW4 (Table 2). Black arrows indicate sample locations and numbers.

Fig. 6. Bedded iron sequences from SW5a at the mine site on the western side of Wadi El-Dabbah between RW11 and RW12.

A: Photograph of a well-preserved, well-exposed, and laterally continuous iron sequence. The view shows the uppermost stratigraphic part containing the massive magnetite-rich iron sequence (sample 160320-46) and the upper part of the hematite-rich iron sequence (samples 160320-36 to -45). The lower talas is a diabase sill. Altered volcaniclastic rocks conformably overlie the iron sequence.

B: Close-up view of the hematite-rich iron sequence in Fig. 6A (i.e., of the white arrow). A hematite-rich bed contains nodular red jasper layers. The parallel laminations of iron–silica–jasper are a few millimeters in thickness.

C-1: Close-up view of a sample chip from the massive magnetite-rich iron sequence (sample 160320-46). This lithology is homogeneous and partly bedded.

C-2: Back-scattered electron image of the massive magnetite-rich iron sequence (sample 160320-46). Fine-grained magnetite is evenly distributed in the sample. The inset shows the location of the close-up view in C-3.

C-3: Enlarged back-scattered electron image of the massive magnetite-rich iron sequence (sample 160320-46). Euhedral and unaltered cubic magnetite is present in a quartz matrix. The central dark area and matrix consist of fine-grained quartz and minor apatite grains.

D-1: Close-up view of a sample chip from the hematite-rich iron sequence (sample 160320-06). The dark brown laminations are hematite and the black and yellow laminations are magnetite-rich. A red jasper layer is also well-preserved within the hematite.

D-2: Back-scattered electron image of the hematite-rich iron sequence (sample 160320-06) from the middle part of SW5a. The central white lamination consists of hematite and the surrounding black area consists of silica and hematite. The inset shows the location of the close-up view in D-3.

D-3: Enlarged back-scattered electron image of the hematite-rich iron sequence (sample 160320-06). The white area consists of cubic magnetite and platy hematite crystals. Platy hematite crystals have overgrown the cubic magnetite crystals. The dark area is silica-rich and contains some apatite.

Fig. 7. Detail view of the black and greenish shale from SW3a and SW4 on the western side of Wadi El-Dabbah along RW12.

A-1: Rock chip from the massive magnetite-rich iron sequence (sample 150321-11) in the uppermost part of section SW3a.

A-2: Thin-section photomicrograph of the massive magnetite-rich iron sequence under plane-polarized light. Black fine-grained magnetite in the matrix is well-preserved and contains spheroidal quartz grains (sample 150321-11).

B-1: Rock chip of the hematite-rich iron sequence (sample 150321-22) in the upper part of section SW4.

B-2: Thin-section photomicrograph of a fine-grained part of the hematite-rich iron sequence under plane-polarized light. Fine-grained quartz and plagioclase are preserved within a massive, fine-grained, magnetite matrix (sample 150321-22).

C-1: Rock chip of a fine-grained, homogeneous, black iron bed from the graded magnetite-rich iron sequence (sample 150321-19) in the middle part of section SW4.

C-2: Thin-section of the graded magnetite-rich iron sequence (C-1) showing the gradational boundary with shale (sample 150321-19) under plane-polarized light..

C-3: Back-scattered electron image showing the homogeneous distribution of silt-sized cubic magnetite grains in a matrix of fine-grained plagioclase and chlorite (sample 150321-19).

D-1: Rock chip of greenish shale with light-colored layers (sample 150321-18). This rock was collected from below the iron sequence.

D-2: Thin-section photomicrograph of greenish shale (sample 150321-18) under plane-polarized light. The sample contains silt-sized volcanic plagioclase grains.

E-1: Rock chip of laminated, graded, black shale (sample 150321-21) from below the iron sequence in section SW4.

E-2: Thin-section photomicrograph of graded black shale (sample 150321-21), showing silt-sized plagioclase, clay minerals, and black organic matter under plane-polarized light.

Fig. 8. REE+Y diagrams normalized to Post-Archean Australian Shale (PAAS; Poumand et al., 2012) for the iron sequence and shale samples from the El-Dabbah Group. Data for DB-141, D12-10, and D13-17b are from El-Shazly et al. (2019).

Fig. 9. Plot of Fe/Ti vs. Al/(Al+Fe+Mn+Na+K+Ca) after Bostrom (1970), Cox et al. (2013), and Abd El-Rahman et al. (2019). End-member compositions of hydrothermal precipitates are from Marchig and Gundlach (1982). Upper continental crust (UCC) line is from Cribb and Barton (1996); shale (PAAS), mid-ocean ridge basalt (MORB), and volcanogenic sediment lines are from Taylor and McLennan (1985); loess line is from Taylor et al. (1983).

Fig. 10. Plot of Ni/Co vs. V/(V+Ni) (after Rimmer, 2004).

Fig. 11. Conceptual model of iron sedimentation in the El-Dabbah Group within the central rift zone. Cyanobacteria bloomed near the ocean surface and low-temperature hydrothermal fluids were derived from the rift area. During periods of volcanic quiescence, hemipelagic shale, black shale, and some iron sequences were deposited within a small basin in the rift zone.

Table 1. Major element data for the iron sequence and shale samples.

Table 2. Rare earth element (REE) data for the iron sequence and shale samples from the El-Dabbah Group.

Table 3. Total organic carbon (TOC) and $\delta^{13}C_{org}$ (‰) values for black shales in the SW4 section.

Fig. 1

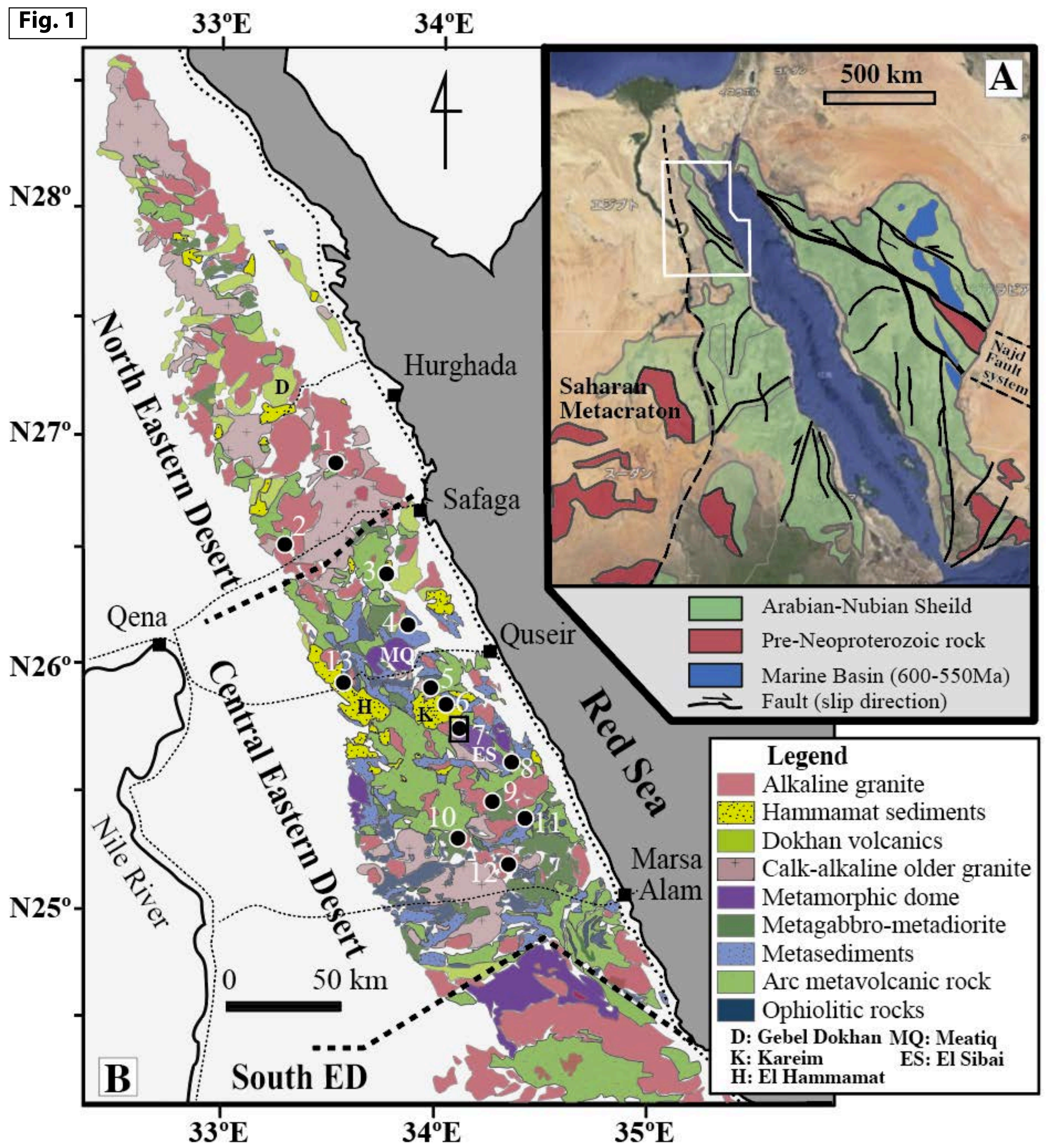
33°E
34°E
35°E
N28°
N27°
N26°
N25°
North Eastern Desert
Central Eastern Desert
Nile River
Hurghada
Safaga
Qena
Quseir
Marsa Alam
Red Sea
D
1
2
3
4
5
6
7
8
9
10
11
12
13
MQ
H
K
C
ES
0
50 km
B
South ED
500 km
A
Saharan Metacraton
Najd Fault system
Arabian-Nubian Sheild
Pre-Neoproterozoic rock
Marine Basin (600-550Ma)
Fault (slip direction)
Legend
Alkaline granite
Hammamat sediments
Dokhan volcanics
Calk-alkaline older granite
Metamorphic dome
Metagabbro-metadiorite
Metasediments
Arc metavolcanic rock
Ophiolitic rocks
D: Gebel Dokhan
MQ: Meatiq
K: Kareim
ES: El Sibai
H: El Hammamat

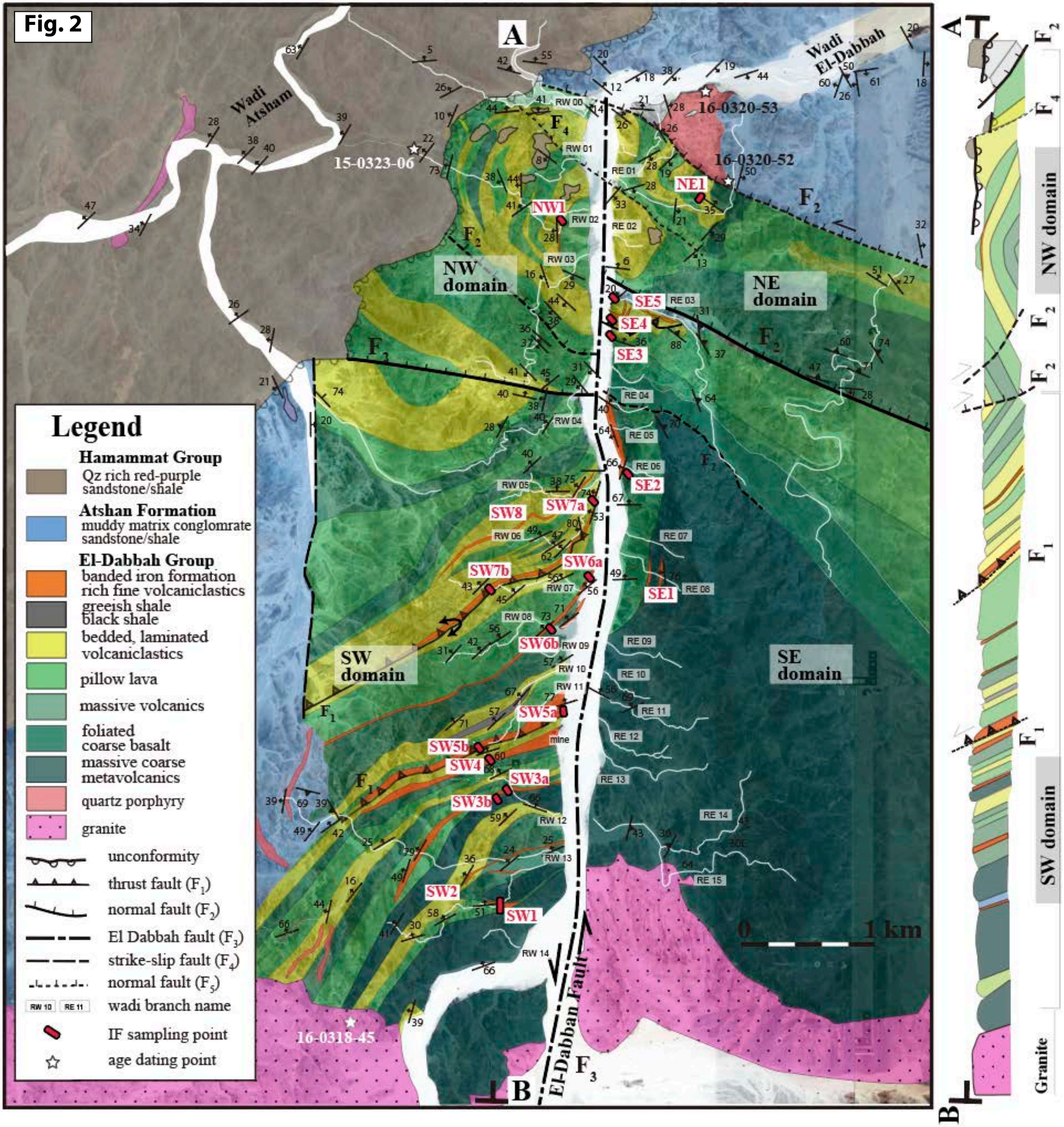
Fig. 2
A
B
Wadi Atsham
Wadi El-Dabbah
15-0323-06
16-0320-53
16-0320-52
16-0318-45
NW domain
NE domain
SW domain
SE domain
El-Dabbah Fault
0 1 km
Legend
Hamammat Group
Qz rich red-purple sandstone/shale
Atshan Formation
muddy matrix conglomrate sandstone/shale
El-Dabbah Group
banded iron formation
rich fine volcaniclastics
greeish shale
black shale
bedded, laminated volcaniclastics
pillow lava
massive volcanics
foliated coarse basalt
massive coarse metavolcanics
quartz porphyry
granite
unconformity
thrust fault (F1)
normal fault (F2)
El Dabbah fault (F3)
strike-slip fault (F4)
normal fault (F5)
wadi branch name
IF sampling point
age dating point
NW domain
SW domain
Granite

Fig. 3

Column of the El-Dabbah Formation

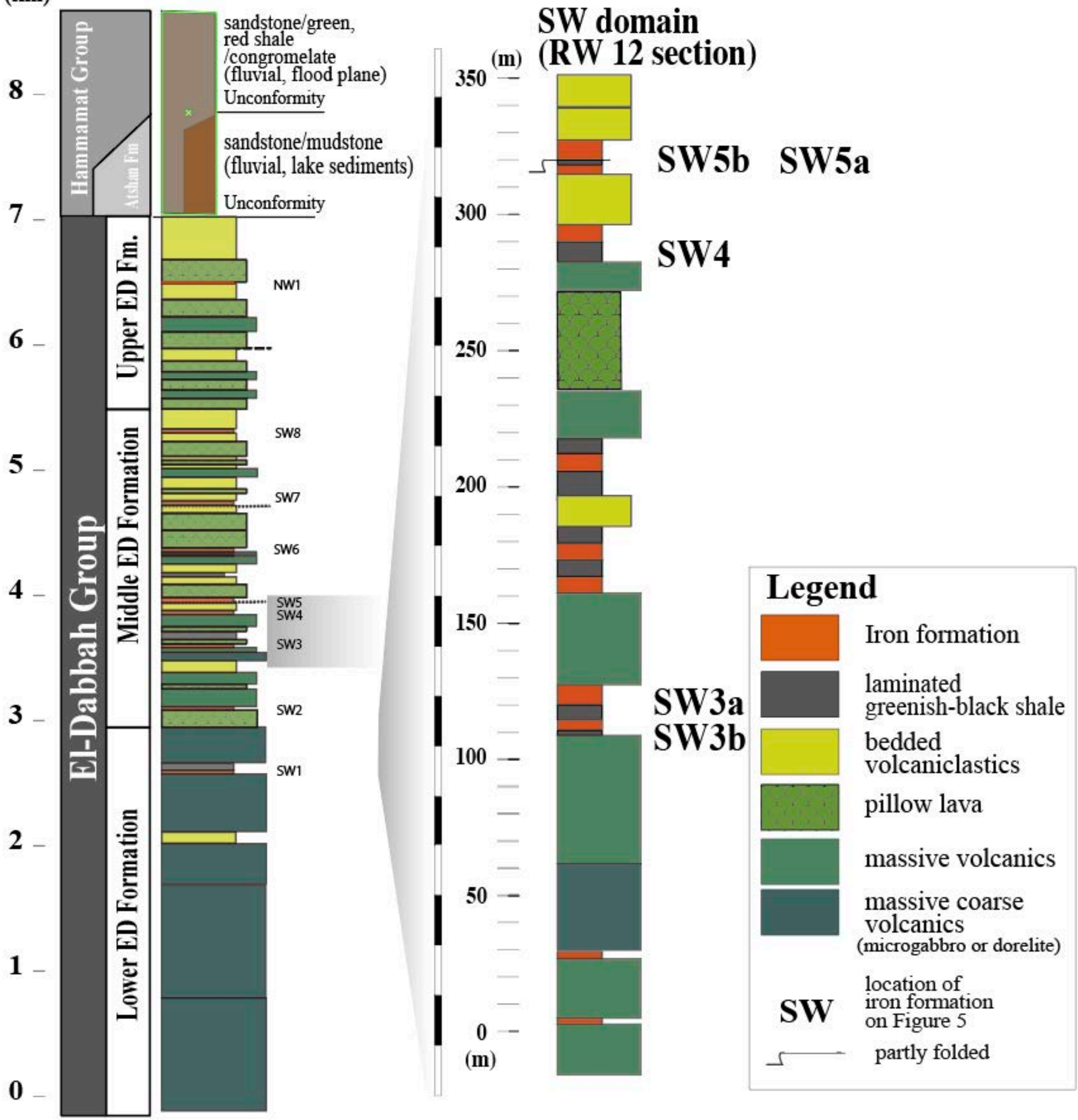

Fig. 4

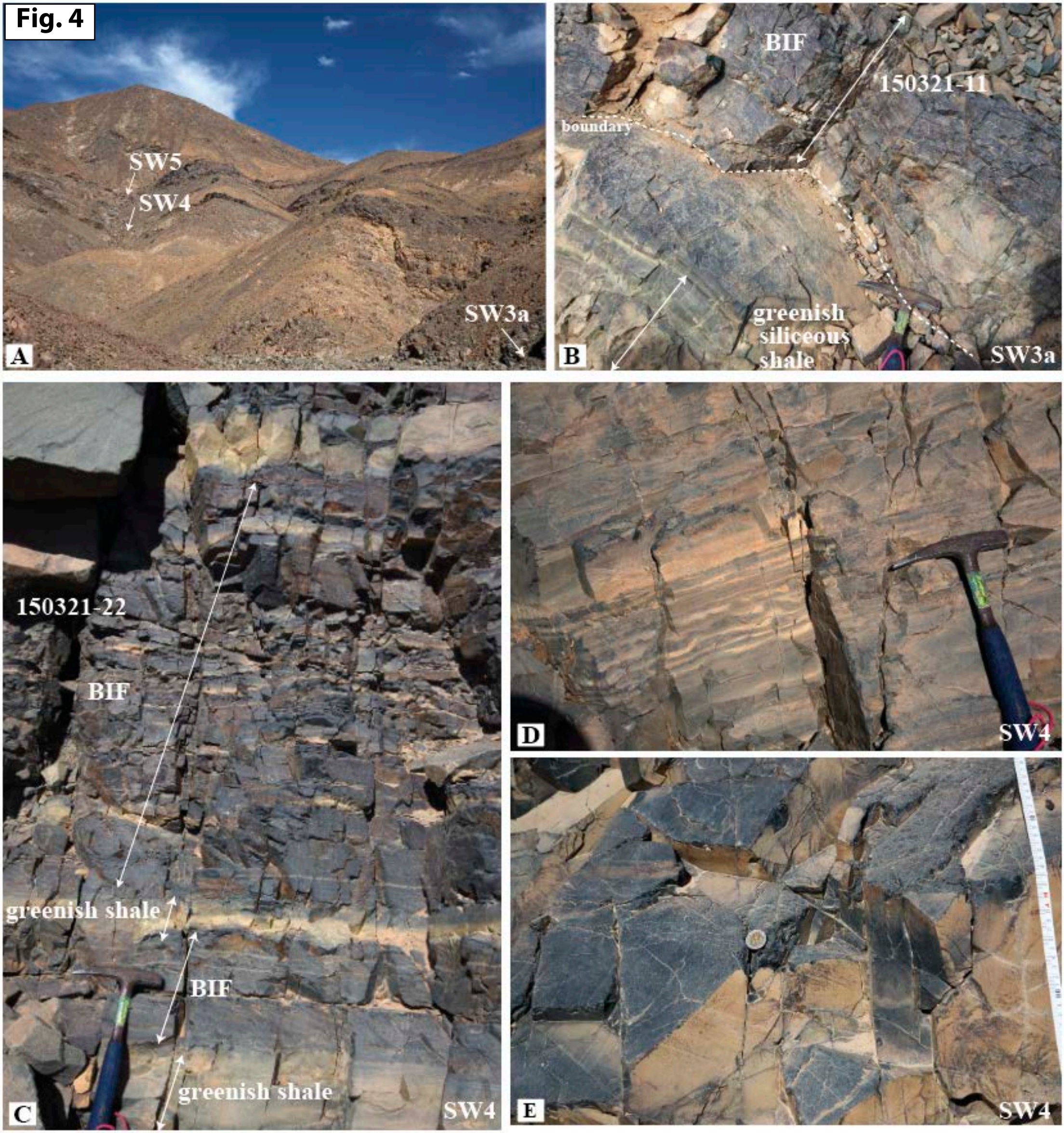
SW5
SW4
SW3a
A
BIF
150321-11
boundary
greenish
siliceous
shale
SW3a
B
150321-22
BIF
greenish shale
BIF
greenish shale
C
SW4
D
SW4
E
SW4

Fig. 5

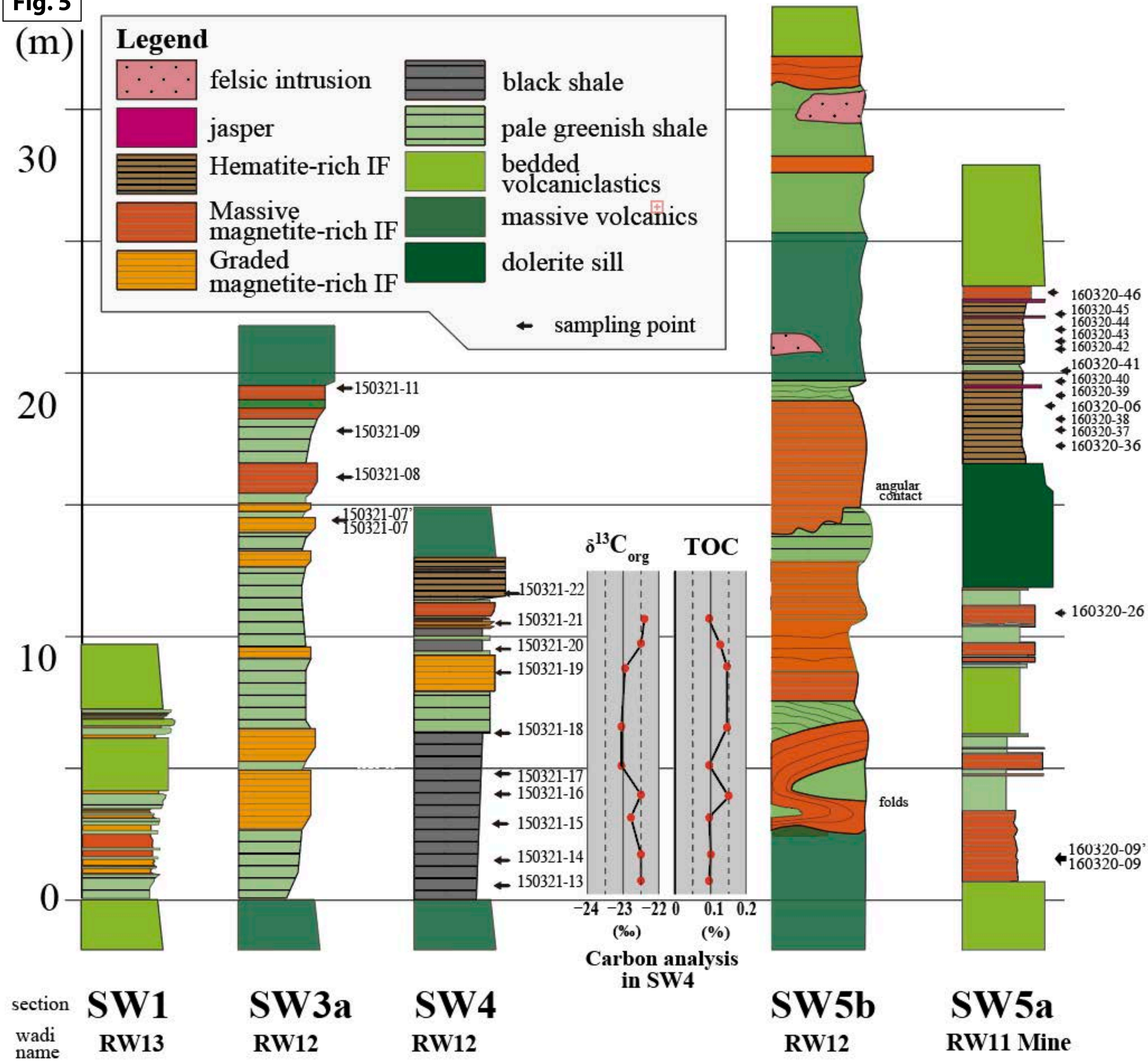
(m)
Legend
felsic intrusion
jasper
Hematite-rich IF
Massive magnetite-rich IF
Graded magnetite-rich IF
black shale
pale greenish shale
bedded volcaniclastics
massive volcanics
dolerite sill
sampling point
30
20
10
0
150321-11
150321-09
150321-08
150321-07'
150321-07
150321-22
150321-21
150321-20
150321-19
150321-18
150321-17
150321-16
150321-15
150321-14
150321-13
δ13Corg
TOC
−24 −23 −22
(‰)
0 0.1 0.2
(%)
Carbon analysis in SW4
angular contact
folds
160320-46
160320-45
160320-44
160320-43
160320-42
160320-41
160320-40
160320-39
160320-06
160320-38
160320-37
160320-36
160320-26
160320-09'
160320-09
section
SW1
SW3a
SW4
SW5b
SW5a
wadi name
RW13
RW12
RW12
RW12
RW11 Mine

Fig. 6

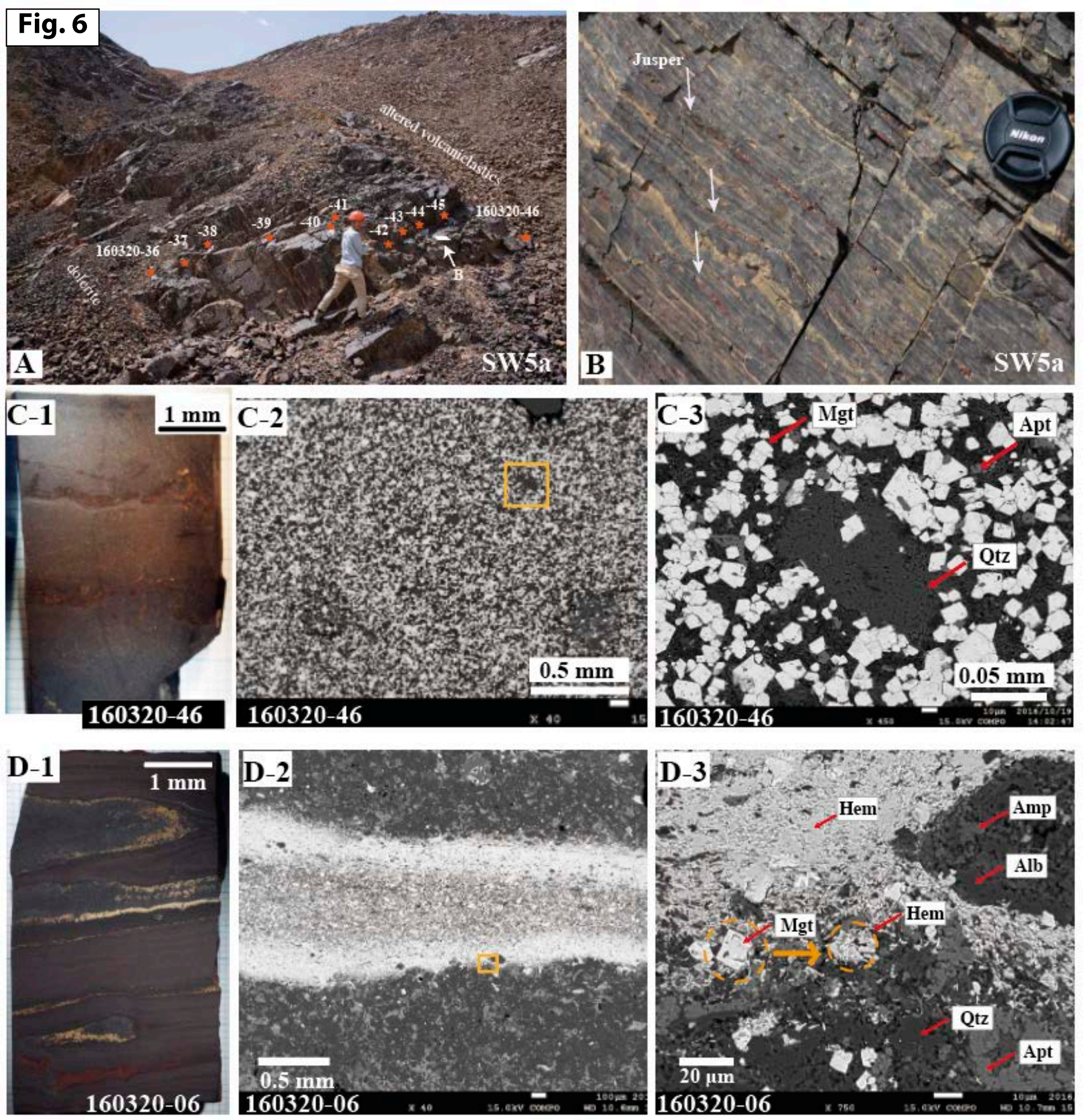
A
SW5a
altered volcaniclastics
dolerite
160320-36
-37
-38
-39
-40
-41
-42
-43
-44
-45
160320-46
B
B
SW5a
Jasper
C-1
1 mm
160320-46
C-2
0.5 mm
160320-46
C-3
Mgt
Apt
Qtz
0.05 mm
160320-46
D-1
1 mm
160320-06
D-2
0.5 mm
160320-06
D-3
Hem
Amp
Alb
Mgt
Hem
Qtz
Apt
20 µm
160320-06

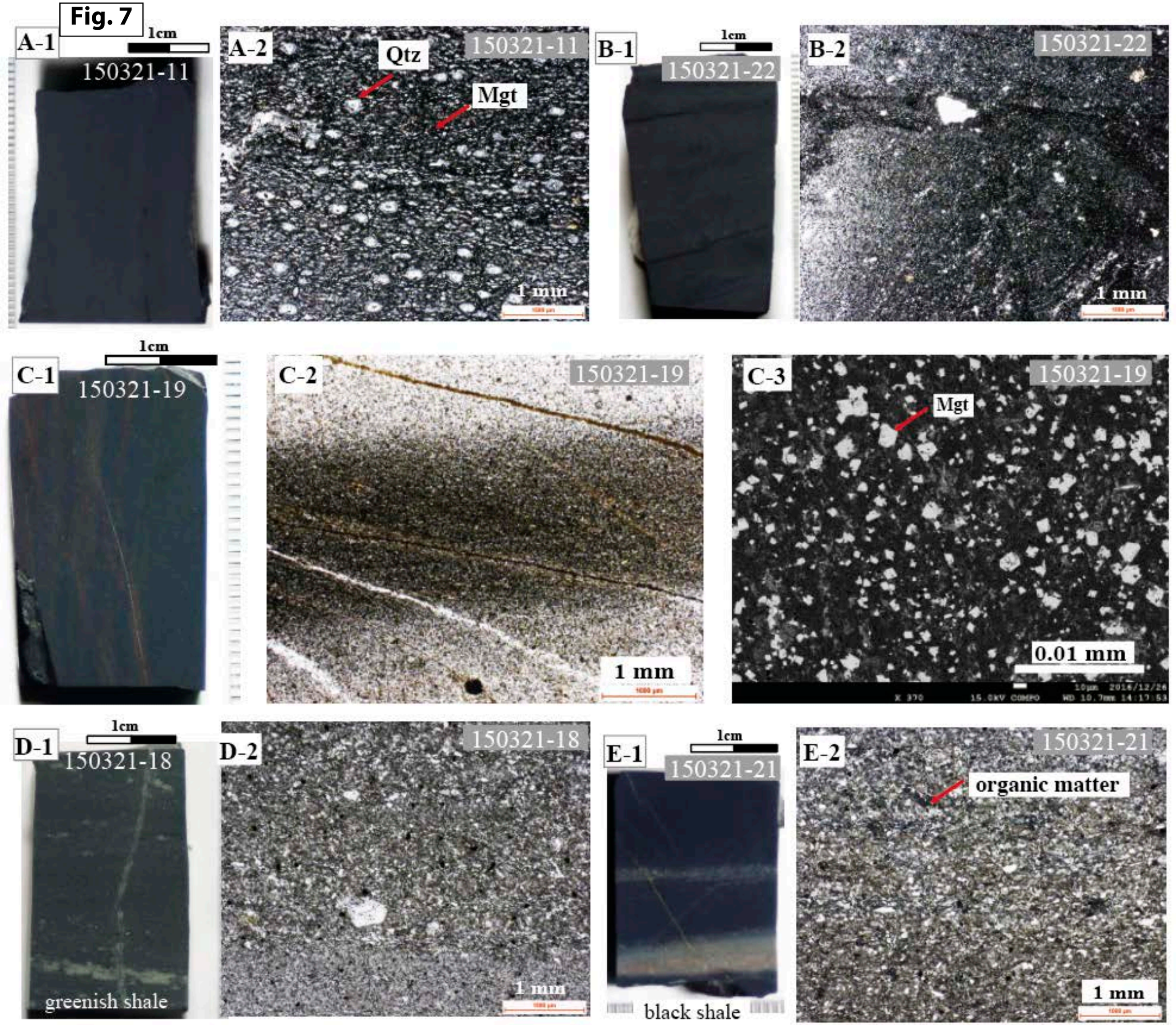
Fig. 7
A-1
1cm
150321-11
A-2
Qtz
Mgt
150321-11
1 mm
B-1
1cm
150321-22
B-2
150321-22
1 mm
C-1
1cm
150321-19
C-2
150321-19
1 mm
C-3
150321-19
Mgt
0.01 mm
D-1
1cm
150321-18
greenish shale
D-2
150321-18
1 mm
E-1
1cm
150321-21
black shale
E-2
150321-21
organic matter
1 mm

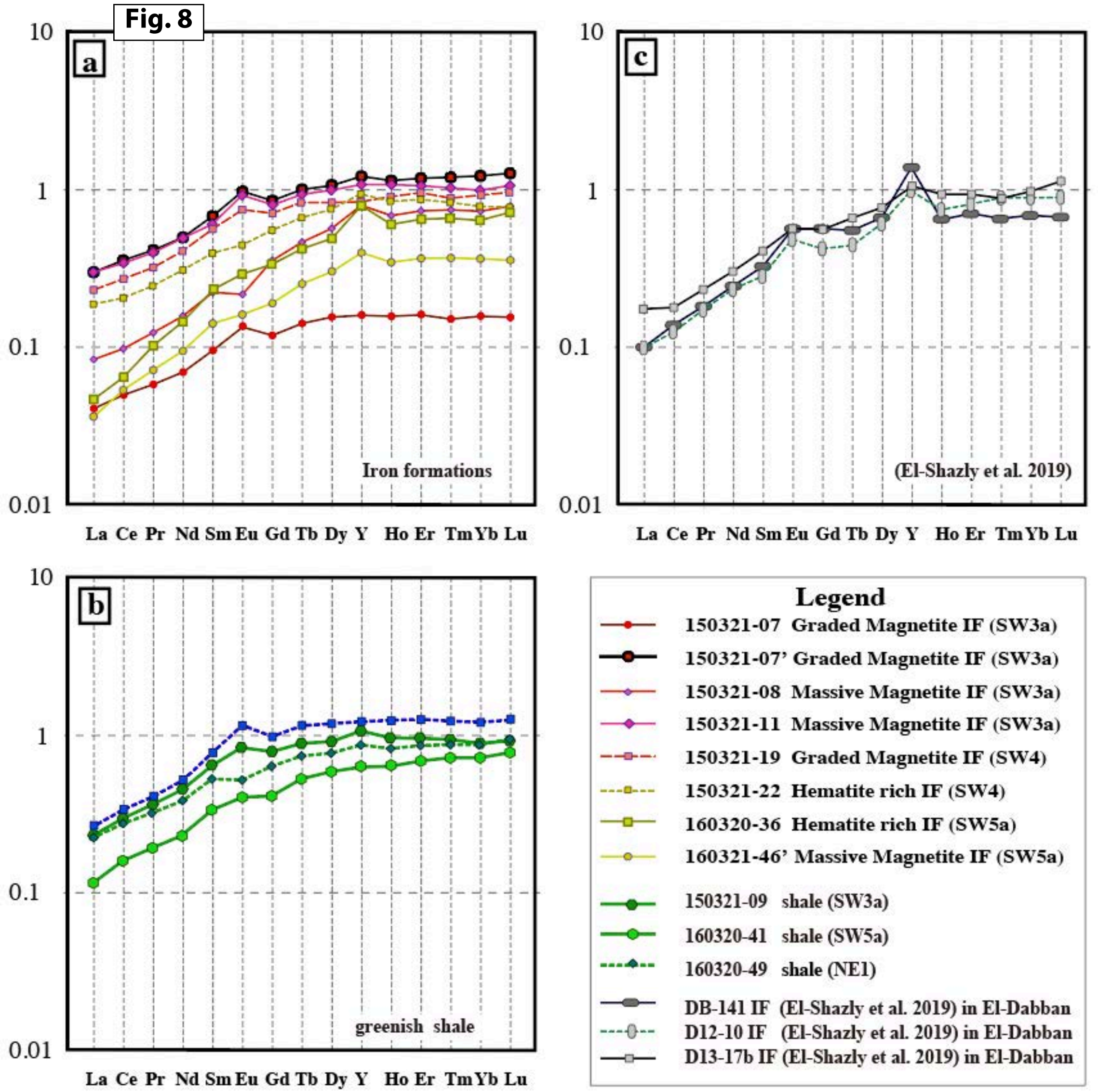
Fig. 8
a
Iron formations
b
greenish shale
c
(El-Shazly et al. 2019)
10
1
0.1
0.01
La Ce Pr Nd Sm Eu Gd Tb Dy Y Ho Er Tm Yb Lu
Legend
150321-07 Graded Magnetite IF (SW3a)
150321-07' Graded Magnetite IF (SW3a)
150321-08 Massive Magnetite IF (SW3a)
150321-11 Massive Magnetite IF (SW3a)
150321-19 Graded Magnetite IF (SW4)
150321-22 Hematite rich IF (SW4)
160320-36 Hematite rich IF (SW5a)
160321-46' Massive Magnetite IF (SW5a)
150321-09 shale (SW3a)
160320-41 shale (SW5a)
160320-49 shale (NE1)
DB-141 IF (El-Shazly et al. 2019) in El-Dabban
D12-10 IF (El-Shazly et al. 2019) in El-Dabban
D13-17b IF (El-Shazly et al. 2019) in El-Dabban

Fig. 9

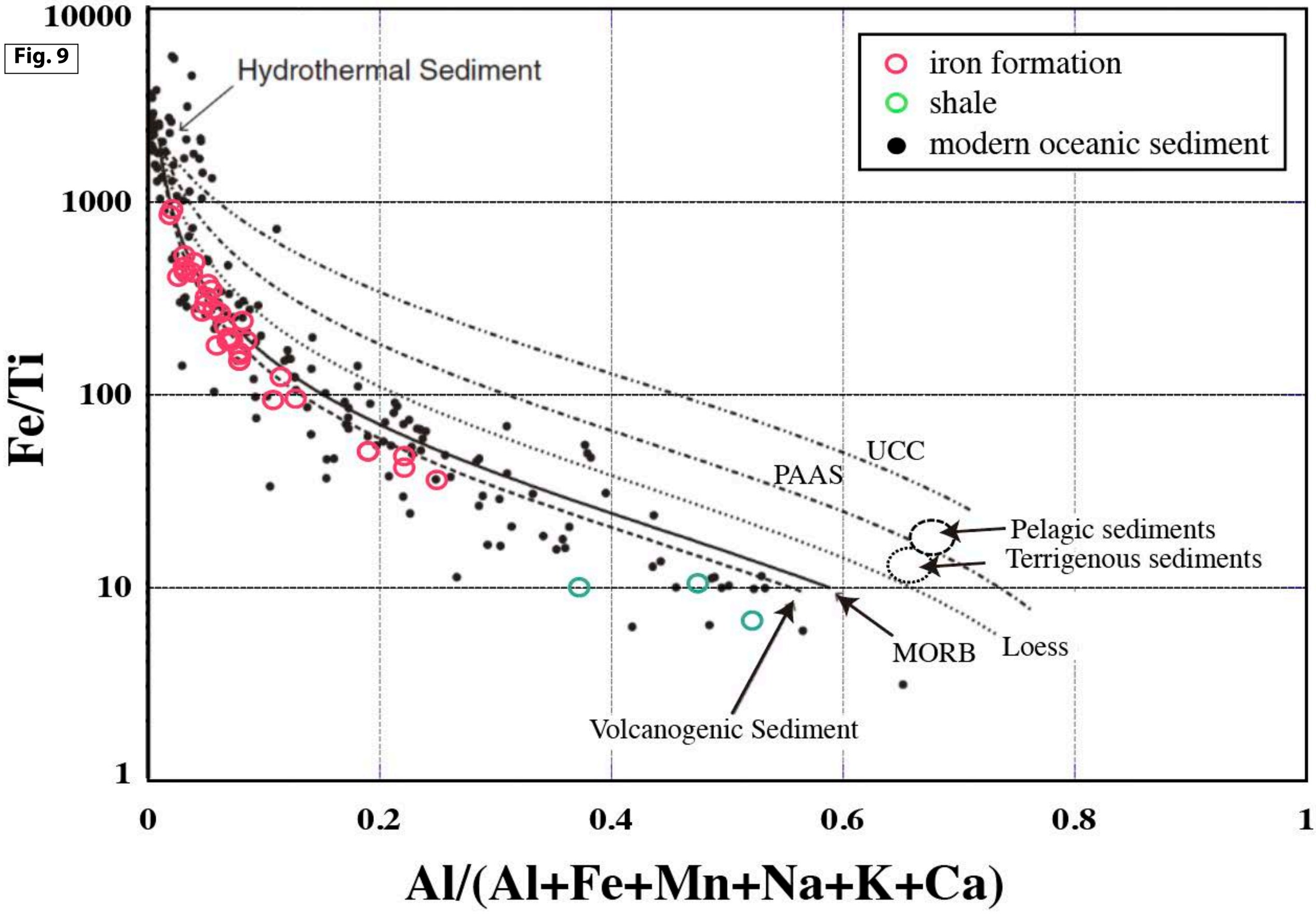
Hydrothermal Sediment
iron formation
shale
modern oceanic sediment
UCC
PAAS
Pelagic sediments
Terrigenous sediments
MORB
Loess
Volcanogenic Sediment
10000
1000
100
10
1
Fe/Ti
0
0.2
0.4
0.6
0.8
1
Al/(Al+Fe+Mn+Na+K+Ca)

Fig. 10

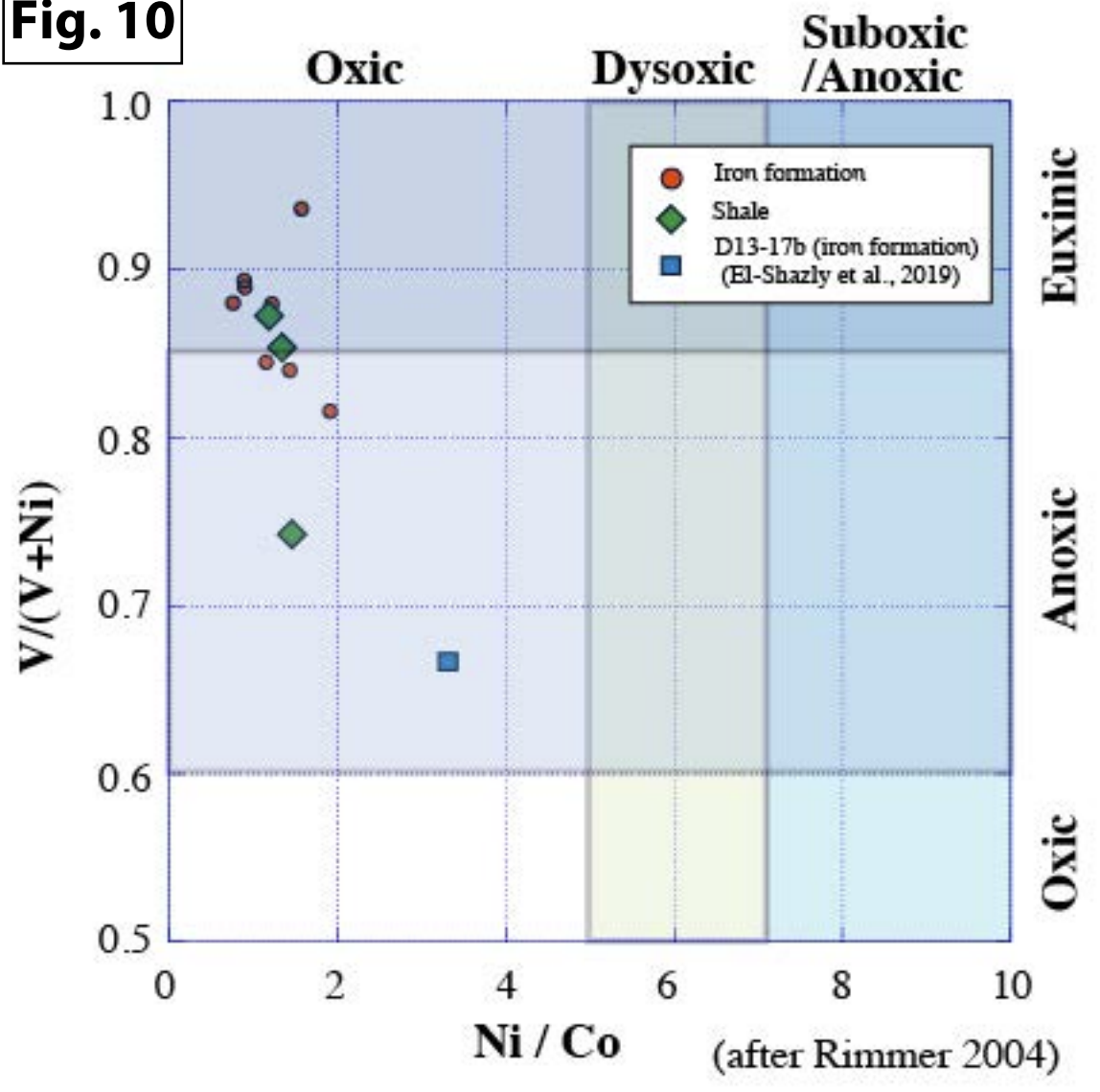
Oxic
Dysoxic
Suboxic /Anoxic
Euxinic
Anoxic
Oxic
Iron formation
Shale
D13-17b (iron formation) (El-Shazly et al., 2019)
V/(V+Ni)
1.0
0.9
0.8
0.7
0.6
0.5
0
2
4
6
8
10
Ni / Co
(after Rimmer 2004)

Oceanic Island arc section

Fig. 11

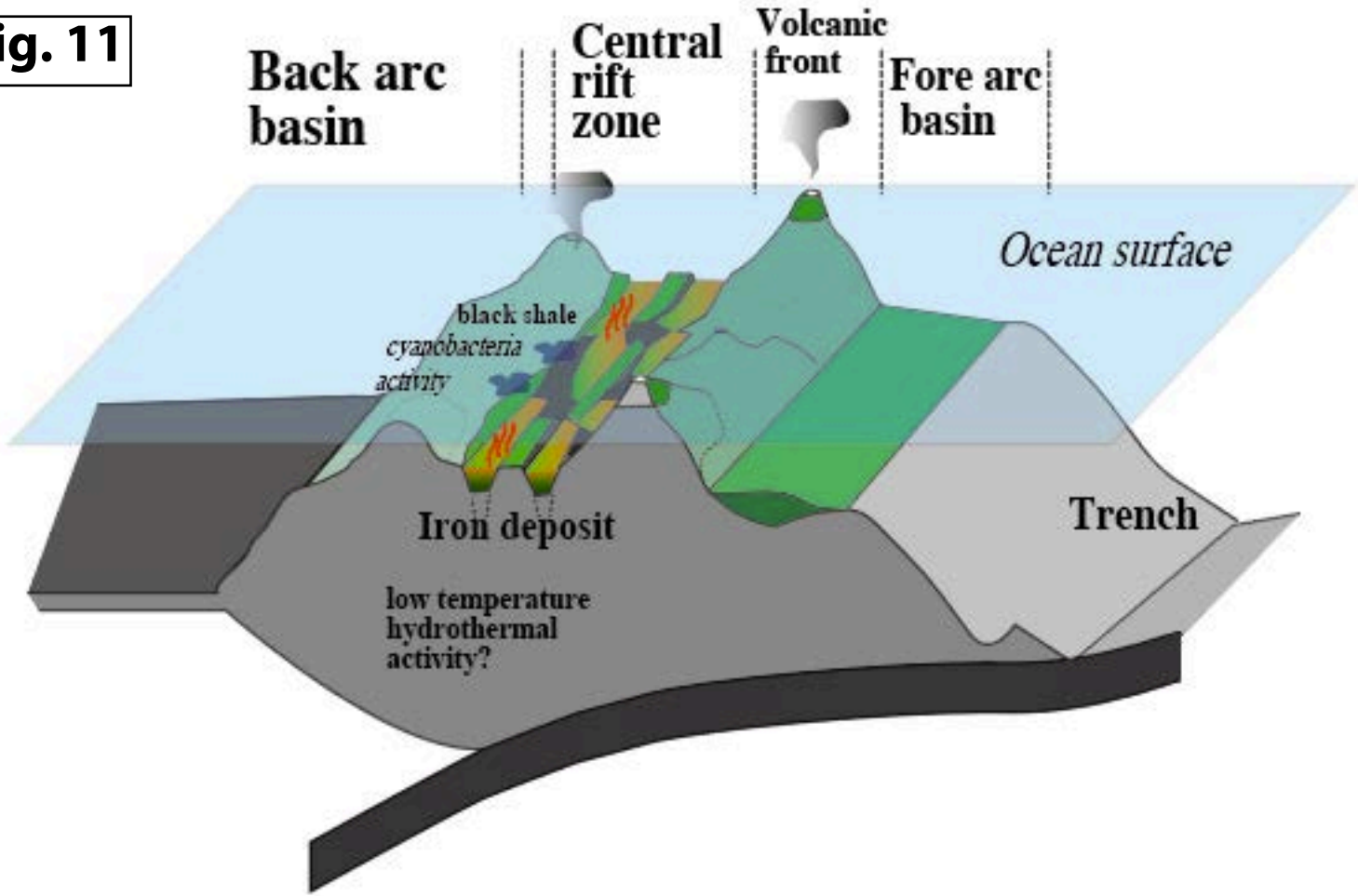

Table 1

Major elements (wt. %)	Graded magnetite-rich IF	Graded magnetite-rich IF	Graded magnetite-rich IF	Massive magnetite-rich IF	Massive magnetite-rich IF	Graded magnetite-rich IF	Hematite-rich IF	Graded magnetite-rich IF	Graded magnetite-rich IF	Graded magnetite-rich IF	Hematite-rich IF	Hematite-rich IF
Sample number	150321-02	150321-07	150321-07'	150321-08	150321-11	150321-19	150321-22	160320-09	160320-09'	160320-26	160320-36	160320-37
section	SW3b	SW3a	SW3a	SW3a	SW3a	SW4	SW4	SW5a	SW5a	SW5a	SW5a	SW5a
location	RW12	RW12	RW12	RW12	RW12	RW12	RW12	RW11 mine	RW11 mine	RW11 mine	RW11 mine	RW11 mine
SiO2	46.67	50.15	47.83	37.64	44.87	45.38	30.21	45.09	43.68	52.84	21.94	16.99
TiO2	0.49	0.63	0.61	0.2	0.2	0.52	0.19	0.22	0.21	0.23	0.17	0.14
Al2O3	8.85	10.11	9.39	3.55	2.62	7.88	3.7	3.46	3.47	3.34	1.94	2.46
Fe2O3	23.85	23.02	25.72	45.86	36.33	26.75	50.72	42.04	42.02	34.90	70.24	74.47
MnO	0.08	0.08	0.09	0.06	0.05	0.05	0.04	0.02	0.03	0.02	0.03	0.02
MgO	1.86	2.22	2.3	1.71	1.38	1.11	1.71	1.02	1.03	1.23	1.29	1.3
CaO	2.57	2.06	2.04	2.08	3.45	3.07	3.04	2.35	2.60	1.74	1.45	1.53
Na2O	0.80	2.12	2.13	0.59	0.49	0.18	0.42	1.50	1.30	0.57	0.06	0.32
K2O	2.13	1.05	0.92	0.2	0.1	2.52	0.39	0.12	0.13	0.80	0.36	0.25
P2O5	1.14	0.65	0.68	1.48	1.8	0.8	2.64	1.64	1.67	1.21	0.84	0.83
LOI	2.48	2.38	3.30	3.87	1.35	3.79	2.33	0.86	1.55	1.57	1.95	2.16
total	90.92	94.47	95.01	97.24	92.64	92.05	95.39	98.32	97.69	98.45	100.27	100.47
SiO2/Al2O3	5.27	4.96	5.09	10.60	17.13	5.76	8.16	13.03	12.59	15.82	11.31	6.91

Major elements (wt. %)	Hematite-rich IF	Hematite-rich IF	Hematite-rich IF	Hematite-rich IF	Hematite-rich IF	Hematite-rich IF	Hematite-rich IF	Massive magnetite-rich IF	Massive magnetite-rich IF	Massive magnetite-rich IF	Massive magnetite-rich IF	Graded magnetite-rich IF
Sample number	160320-38	160320-39	160320-40	160320-42	160320-43	160320-44	160320-45	160320-46	160320-46'	150322-06	160321-50	150323-10
section	SW5a	SW5a	SW5a	SW5a	SW5a	SW5a	SW5a	SW5a	SW5a	SW6b	SW7a	NW1
location	RW11 mine	RW11 mine	RW11 mine	RW11 mine	RW11 mine	RW11 mine	RW11 mine	RW11 mine	RW11 mine	RW08	RW06	RW03
SiO2	22.16	20.25	24.44	27.07	12.13	15.7	18.72	24.19	22.2	33.46	45.35	36.69
TiO2	0.15	0.14	0.15	0.14	0.18	0.09	0.08	0.22	0.2	0.26	0.24	0.24
Al2O3	2.23	2.98	2.67	2.14	2.71	1.5	1.59	3.94	3.59	4.32	3.75	4.74
Fe2O3	65.71	68.61	65.16	64.9	78.76	77.55	73.57	61.52	64.78	50.16	40.20	46.15
MnO	0.02	0.03	0.03	0.02	0.02	0.01	0.02	0.07	0.07	0.04	0.04	0.06
MgO	1.19	1.46	1.33	1.38	1.64	1.28	1.25	1.79	1.74	1.81	2.00	1.79
CaO	2.69	1.85	1.81	1.54	1.46	1.43	1.54	2.22	2.09	2.32	1.87	2.09
Na2O	0.23	0.45	0.34	0.3	0.13	0.03	0.09	0.15	-0.01	0.89	0.01	1.07
K2O	0.27	0.32	0.31	0.15	0.24	0.17	0.13	0.68	0.58	0.42	0.07	0.25
P2O5	2.49	1.31	1.26	0.99	0.88	0.86	0.95	1.97	1.78	1.15	1.43	1.87
LOI	1.66	2.41	2.22	1.80	2.47	2.55	2.62	2.00	1.59	1.13	2.83	2.70
total	98.8	99.81	99.72	100.43	100.62	101.17	100.56	98.75	98.61	95.96	97.79	97.65
SiO2/Al2O3	9.94	6.80	9.15	12.65	4.48	10.47	11.77	6.14	6.18	7.75	12.09	7.74

Major elements (wt. %)	Massive magnetite-rich IF	Graded magnetite-rich IF	Graded magnetite-rich IF	Graded magnetite-rich IF	Graded magnetite-rich IF	Massive magnetite-rich IF	Shale	Shale	Shale	iron formation	iron formation	iron formation
Sample number	150319-12	150320-16	150320-17	160321-34	160321-10	150318-02	150321-09	160321-41	150321-49	El-Shazly et al. (2019)		
location	SE1	SE2	SE2	SE3	SE4	SE5	SW3a	SW5b	NE1	DB-141	D12-10	D13-17b
	RE08	RE06	RE06	RE03	RE03	RE03	RW12	RW11 mine	RE3	unknown	unknown	unknown
SiO2	48.20	29.87	35.09	29.29	26.52	26.88	61.13	65.64	68.95	41.29	41.21	30.44
TiO2	0.25	0.31	0.46	0.18	0.16	0.20	0.68	0.73	0.46	0.47	0.11	0.22
Al2O3	4.75	4.89	6.02	2.68	3.56	3.33	13.16	15.58	12.83	7.32	2.66	5.71
Fe2O3	31.17	50.39	43.58	49.08	56.36	59.38	6.90	4.99	4.90	45.2	41.57	53.64
MnO	0.06	0.05	0.05	0.07	0.12	0.04	0.14	0.04	0.09	0.12	0.02	0.09
MgO	1.60	1.65	1.71	1.48	1.96	1.22	3.26	1.43	2.09	2.19	0.08	1.52
CaO	2.53	2.78	2.38	4.91	3.42	2.62	8.55	2.08	2.70	0.34	7.11	9.13
Na2O	0.77	1.46	1.25	-0.01	-0.05	1.39	3.28	3.47	1.45	2.46	0.67	0.07
K2O	0.81	0.47	1.03	0.13	0.23	0.16	0.12	2.31	3.00	0.09	0.027	0.1
P2O5	1.07	1.63	1.48	1.87	2.60	2.31	0.13	0.08	0.13	1.8	4.34	1.87
LOI	4.27	2.18	1.41	5.46	2.45	0.13	2.41	4.02	3.55	1.11	1.73	0.71
total	95.48	95.68	94.46	95.14	97.33	97.66	99.76	100.37	100.15	101.4	99.58	103.05
SiO2/Al2O3	10.15	6.11	5.83	10.93	7.45	8.07	4.65	4.21	5.37	5.64	15.49	5.33

Table 2

sample No.		column level (m)	TOC (%)	$\delta^{13}C_{org}$ (‰)
150321-13	SW4	1.1	0.09	-22.5
150321-14	SW4	2.1	0.10	-22.5
150321-15	SW4	3.9	0.09	-22.8
150321-16	SW4	4.9	0.15	-22.5
150321-17	SW4	6.0	0.09	-23.1
150321-18	SW4	7.5	0.14	-23.1
150321-19	SW4	10.0	0.14	-22.9
150321-20	SW4	11.0	0.12	-22.5
150321-21	SW4	12.0	0.09	-22.4